

A Cascadia Slab Model from Receiver Functions

Wasja Bloch¹, Michael G. Bostock¹, Pascal Audet²

This is an non-peer reviewed manuscript submitted to EarthArXiv

¹The University of British Columbia, Vancouver, Canada

²University of Ottawa, Ottawa, Canada

Key Points:

- We model Cascadia subduction stratigraphy as three dipping horizons
- Slab morphology is controlled by crystalline terrane backstops
- A near-ubiquitous ~ 2 – 10 km thick ultra-low velocity zone in tremor zone correlates with E-layer

Abstract

We map the characteristic signature of the subducting Juan de Fuca and Gorda plates along the entire Cascadia forearc from northern Vancouver Island, Canada to Cape Mendocino in northern California, USA, using teleseismic receiver functions. The subducting oceanic crustal complex, possibly including subcreted material, is parameterized by three horizons capable of generating mode-converted waves: a negative velocity contrast at the top of a low velocity zone underlain by two horizons representing positive contrasts. The amplitude of the conversions varies likely due to differences in composition and/or fluid content. We analyzed the slab signature for 298 long-running land seismic stations, estimated the depth of the three interfaces through inverse modeling and fitted regularized spline surfaces through the station control points to construct a margin-wide, double-layered slab model. Crystalline terranes that act as the static backstop appear to form the major structural barrier that controls slab morphology. Where the backstop recedes landward beneath Olympic Peninsula and Cape Mendocino, the slab subducts sub-horizontally, while the seaward-protruding and thickened Siletz terrane beneath central Oregon causes steepening of the slab. A tight bend in slab morphology south of Olympic Peninsula coincides with the location of recurring large intermediate depth earthquakes. The top-to-Moho thickness of the slab generally exceeds the thickness of the oceanic crust by 2-12 km, suggesting thickening of the slab or underplating of slab material to the overriding North American plate.

Plain Language Summary

The tectonic Juan de Fuca plate, that underlies the easternmost North Pacific Ocean off-shore Vancouver Island, Washington, Oregon and northern California, is being pushed beneath the North American continent by plate tectonics. On its way deep into the Earth the plate deforms. In this study, we analyze seismograms of distant earthquakes which were recorded within the study area. Through signal and data processing we decipher information about the location, orientation and properties of the down-going oceanic plate beneath the continent. The data show that the plate protrudes shallowly dipping under the continent beneath Olympic Peninsula (Washington) and Cape Mendocino (California) while it dips down more steeply under central Oregon and Vancouver Island (British Columbia). This configuration suggests that Siletzia, an old and rigid basalt plateau that forms the central part of the study area, controls the shape of the down-going plate. Furthermore, the oceanic plate appears to significantly thicken at depth, which may indicate that parts of it accumulate at the base of the continent. These results are important to better understand the subduction process, and may help to infer the location of the deeper extent of rupture in a future potential strong earthquake.

1 Introduction

The boundary between the down-going oceanic and overriding continental plates in subduction zones is the locus of major seismic moment release in great earthquakes and enigmatic slow earthquakes. Knowledge about its location and characteristics is key to understanding seismogenesis, tsunamigenesis, and geodynamic processes taking place in subduction zones. During the subduction process, the down-going slab is subject to mechanical and chemical alterations, including flexure, shearing, increases in temperature and pressure, metamorphism, fluid generation and redistribution, metasomatism, and other complex geodynamical processes. All of these factors are expected to influence the slab's mechanical behaviour.

In the Cascadia subduction zone, the Juan de Fuca plate (JdF) subducts beneath the North American plate at velocities that vary between 42 mm yr^{-1} at its northern end near the Nootka Fault Zone, to 36 mm yr^{-1} at its southern end, near the Blanco Frac-

60 ture Zone. The plate subducts at an azimuth of $\sim N56^\circ E$. To the south, the Gorda micro-
 61 plate subducts at 33 mm yr^{-1} with an azimuth of $N52^\circ E$ (DeMets et al., 1994). The Ex-
 62 plorer plate to the north does not subduct, but more likely underthrusts the North Amer-
 63 ican Plate beneath northern Vancouver Island (Riddihough, 1984; Audet et al., 2008; Savard
 64 et al., 2020; Merrill et al., 2022). To the north, the subduction system transforms into
 65 the right-lateral Queen Charlotte and Revere-Dellwood Faults; to the south into the San
 66 Andreas Fault (Fig. 1).

67 Immediately landward of the deformation front, the subduction interface can be
 68 identified in high-frequency reflection seismic sections along the entire Cascadia margin
 69 (e.g., Carbotte et al., 2022; Han et al., 2016; Calvert, 1996; Calvert & Clowes, 1991; Flueh
 70 et al., 1998; MacKay et al., 1992; Gulick et al., 1998; Clowes, Yorath, & Hyndman, 1987).
 71 In places, the structural décollement is located within the lower part of the sedimentary
 72 blanket, implying sediment subduction (Han et al., 2016; Tréhu et al., 2012, 1994; Flueh
 73 et al., 1998).

74 Farther downdip, the JdF has been identified below the Salish Sea on marine seis-
 75 mic sounding transects through the Juan de Fuca Strait and Georgia Strait. At about
 76 20 km depth, the sharp $<2 \text{ km}$ thick reflector that marks the top of the slab widens into
 77 an up to 10 km wide reflection band, the so-called E-layer (e.g., Clowes, Brandon, et al.,
 78 1987; Nedimović et al., 2003), that extends to depths of at least $\sim 50 \text{ km}$ (Calvert et al.,
 79 2006). A similarly thick reflective zone has been identified atop the subducting JdF at
 80 35-40 km depth beneath central Oregon (Keach et al., 1989; Tréhu et al., 1994). It has
 81 been argued that the E-layer represents the transition into a wider shear zone that creeps
 82 aseismically and hosts episodic tremor and slip (ETS, see e.g. Calvert et al., 2020; Ned-
 83 imović et al., 2009).

84 At lower frequencies ($\leq 1 \text{ Hz}$), the receiver function method can be used to image
 85 sharp velocity changes such as the Moho or the Conrad interface, low-velocity zones, and
 86 mantle transition zone discontinuities. It has previously been employed to identify dis-
 87 continuities in complex 3-D geological structures worldwide e.g. in the Himalayan belt
 88 (e.g., Caldwell et al., 2013; Singer et al., 2017; Subedi et al., 2018; Xu et al., 2021), the
 89 Alps (e.g., Colavitti et al., 2022; Liu et al., 2022; Michailos et al., 2023), the Andes (e.g.,
 90 Yuan et al., 2000; Bar et al., 2019; Rodriguez & Russo, 2019), and Japan (e.g., Chen et
 91 al., 2005; Li et al., 2000; Niu et al., 2005).

92 In Cascadia, the subduction zone stratigraphy has also been previously been char-
 93 acterized using teleseismic P -wave receiver function data (e.g., Langston & Blum, 1977;
 94 Cassidy & Ellis, 1993; Nabelek et al., 1993; Bostock et al., 2002; Nicholson et al., 2005;
 95 Abers et al., 2009; McGary et al., 2014; Mann et al., 2019). A recent study employing
 96 receiver functions, local tomography and seismic reflection data in southern Vancouver
 97 Island suggests that the oceanic crust may reside below the E-layer (Calvert et al., 2020)
 98 and that at least part of the E-layer comprises an ultra-low S -wave velocity zone (ULVZ),
 99 with V_P/V_S in the order of 2–3 (Audet et al., 2009; Cassidy & Ellis, 1993). In local seis-
 100 mic tomograms, the slab stratigraphy oftentimes appears smeared into a single layer with
 101 moderately elevated V_P/V_S in the order of 1.8–2.0, consistent with basaltic or gabbroic
 102 lithologies with some contribution of fluid-filled pores. Interpretation of the oceanic Moho
 103 in tomographic models is less ambiguous, where it appears as a strong negative V_P/V_S
 104 gradient to values below 1.7 that mark the oceanic mantle below (Guo et al., 2021; Mer-
 105 rill et al., 2020, 2022; Savard et al., 2018).

106 An initial margin-wide map of the top of the JdF was constructed from a mixed
 107 dataset of earthquake hypocenters, active source seismic profiles, receiver functions and
 108 local earthquake tomograms with the aim to model interseismic strain accumulation in
 109 the overriding plate (Flück et al., 1997). With increasing data availability over time and
 110 a better understanding of subduction processes, the initial model has been updated and
 111 extended in space using additional constraints from seafloor magnetic anomalies, deeper

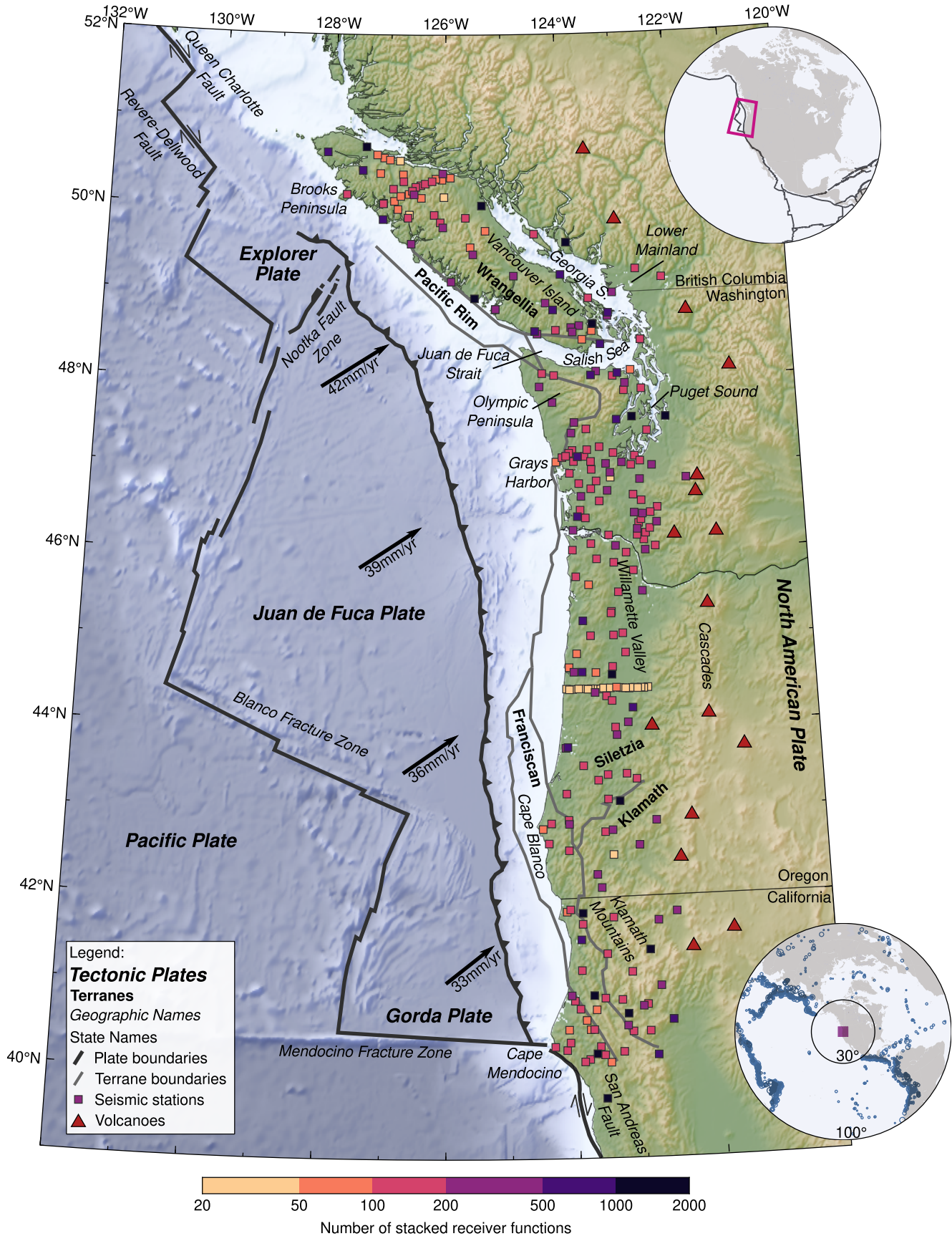


Figure 1. Tectonic setting of the Cascadia subduction zone and station distribution employed to determine the slab geometry under the forearc. Convergence of the Juan de Fuca and Gorda Plates relative to stable North America shown as arrows (DeMets et al., 1994). Terrane boundaries modified after Watt & Brothers (2020). Top inset: Location of the study area on the North American continent. Bottom inset: Earthquake source distribution from 30° to 100° epicentral distance used to compute receiver functions.

112 seismicity and diffraction of strong earthquake first arrivals (McCrory et al., 2004) and
 113 later from relocated earthquake hypocenters and electrical conductivity profiles (Hayes
 114 et al., 2018; McCrory et al., 2012). Other slab models are based purely on receiver func-
 115 tions (Audet et al., 2010; Hansen et al., 2012).

116 Despite a broad agreement in recovered slab depths to within ~ 10 km, consider-
 117 able differences exist across these models. These differences are associated with data un-
 118 certainties, the fact that the slab models are based on different data types, and with am-
 119 biguities in the interpretation of proxies for what constitutes the “slab top” (McCrory
 120 et al., 2012).

121 Here, we construct a margin-wide slab model that honors an oceanic crustal stratig-
 122 raphy including the possibility of subcreted material that may consist of up to two lay-
 123 ers. Our model is based on the observation that receiver function images of the slab ex-
 124 hibit characteristic successions of positively and negatively polarized conversions that
 125 can be explained by interfering forward- and back-scattered seismic wave modes orig-
 126 inating at three interfaces. We map these interfaces continuously along dip from the coast
 127 to the forearc lowlands (Salish Sea, Willamette Valley) and along strike from Brooks Penin-
 128 sula on northern Vancouver Island, Canada, to Cape Mendocino, USA (Fig. 1). Our re-
 129 sults demonstrate how the overall slab morphology is controlled by the location of the
 130 static backstop. A subduction stratigraphy that is generally thicker than the incoming
 131 oceanic crust is testament to complex deformation processes affecting slab morphology
 132 along the subduction trajectory.

133 2 Data and Methods

134 A total of 45,601 individual receiver functions recorded at 298 seismic stations dis-
 135 tributed across the Cascadia forearc contributed to the slab model. For each station, 100 s
 136 recordings symmetric about the P -wave arrival (i.e. 50 s noise and 50 s signal, for con-
 137 venience) of earthquakes with magnitudes between 5.5 and 8, in the distance range be-
 138 tween 30 and 100° , were downloaded (Fig. 1). Waveforms with a signal-to-noise ratio
 139 smaller than 5 dB on the vertical component or 0 dB on the radial component were ex-
 140 cluded. The instrument responses were removed and the seismograms were transformed
 141 to the upgoing P - SH - SV modes (Kennett, 1991). The P -component was trimmed to
 142 the time window beyond which the envelope fell below 2% of the maximum amplitude
 143 and a cosine taper was applied.

144 2.1 Receiver function processing

145 The three component P -wave spectra were scaled by their signal-to-noise ratio and
 146 binned according to their incidence angle in back-azimuth bins of 7.5° and horizontal slow-
 147 ness bins of 0.002 s km^{-1} . Within each bin, radial and transverse receiver functions were
 148 computed through frequency-domain simultaneous deconvolution (Gurrola et al., 1995),
 149 with an optimal damping factor found through generalized cross validation (Bostock, 1998).

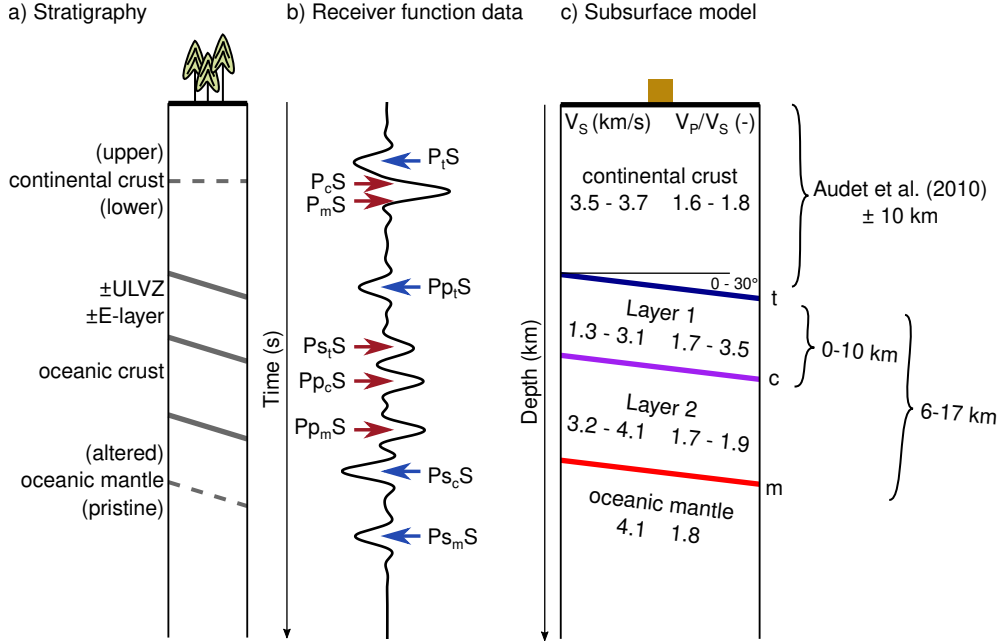


Figure 2. a) Forearc stratigraphy with the previously identified interfaces. b) Schematic radial receiver function with the forward and back scattered mode conversions used to constrain the model. Phases may interfere and cancel out in some cases. Absence of specific phase combinations may therefore be meaningful. Upper case letters indicate up-going rays, lower case letters down-going rays, subscript the scattering interface. c) Parameterization of the subsurface model. The possible presence of additional interfaces complicates the phase associations.

150 This approach mitigates the instabilities inherent in spectral division by stacking spec-
 151 tra prior to deconvolution.

152 **2.2 Parameter search**

153 The continental forearc and subducting slab were parameterized as three layers over
 154 a mantle half-space, with the subduction stratigraphy bounding interfaces labelled as t
 155 (t top), c (central) and m (Moho) (Fig. 2). Synthetic receiver functions were calculated
 156 through ray-theoretical modeling of plane-wave scattering at the model interfaces (Fred-
 157 eriksen & Bostock, 2000; Bloch & Audet, 2023, Fig. 2b). The thickness, S -wave velocity
 158 (V_S) and P - to S -wave velocity ratio (V_P/V_S) of each layer, as well as the common
 159 strike and dip of the bottom two layers and the top of the half space (in total 11 param-
 160 eters) were optimized simultaneously through a simulated annealing global parameter
 161 search scheme (Xiang et al., 1997), as implemented in the *SciPy* package (Virtanen et
 162 al., 2020). In analogy to the annealing process in metallurgy, the scheme samples the mis-
 163 fit function stochastically under a decreasing “temperature” that gradually favours low-
 164 misfit parameter combinations. In this way the algorithm can escape local minima in the
 165 misfit function. It has proven efficient in converging toward the global minimum in prob-
 166 lems with many independent variables (Kirkpatrick et al., 1983). The misfit was defined
 167 as the anti-correlation (1 minus the cross correlation coefficient) between the observed
 168 and predicted receiver functions, bandpass filtered between 2 and 20 s period duration.

169 Initial thickness bounds for the continental crust (Fig. 2c) were based on the slab
 170 model of Audet et al. (2010) (± 10 km). Maximum Layer 1 thickness was constrained by

171 the maximum E-layer thickness of 10 km (Nedimović et al., 2003), maximum Layer 2 thick-
 172 ness with the thickness of the incoming oceanic crust of 6.5 km (Han et al., 2016). Layer 1
 173 could attain zero-thickness if the E-layer were absent. Because the igneous oceanic crust
 174 may be part of the E-layer, Layers 1 and 2 were constrained to have a combined min-
 175 imum thickness of 6 km. Velocity bounds (Fig. 2c) for the continental crust and Layer 2
 176 were based on the 2σ interval of the expected lithologies for continental and oceanic crust,
 177 respectively, from the seismic velocity database of Christensen (1996); and for Layer 1
 178 on an analytic poro-elastic model (Bloch et al., 2018) constrained to match the V_P/V_S
 179 observations of the ULVZ (Audet et al., 2009).

180 To verify convergence toward a global minimum, the global parameter search was
 181 initialized with at least three different random number seeds, which affect the distribu-
 182 tion from which trial parameter estimates are drawn. The resulting data predictions and
 183 models were checked for consistency with neighboring stations, previous tomographic pro-
 184 files (Guo et al., 2021; Kan et al., 2023; Merrill et al., 2020; Savard et al., 2018), hypocen-
 185 tral locations of low-frequency earthquakes (LFEs) within tremor (Plourde et al., 2015;
 186 Royer & Bostock, 2014; Armbruster et al., 2014; Savard et al., 2020, 2018) and offshore
 187 marine seismic profiles (Suzanne Carbotte, pers. comm; Carbotte et al., 2023). If none
 188 of the minimum misfit models of an individual station were consistent with the above
 189 constraints, the global search was repeated within narrower bounds around a preferred
 190 solution from a neighboring, reliable station. Such a model was only used in case it con-
 191 verged toward values away from thickness bounds (Fig. 3). For each of the three hori-
 192 zons, a quality and a nominal depth uncertainty were assigned. Quality *A* denotes a hori-
 193 zon where at least one back-scattered phase in the predicted data correlates with the ob-
 194 served data (Fig. 3a and b), the predicted data are consistent among neighboring sta-
 195 tions and the modeled horizon depth is consistent with the available external constraints.
 196 A quality *B* horizon shows a good phase correlation, but the predicted data are incon-
 197 sistent with neighboring stations and/or the modeled depth is inconsistent with exter-
 198 nal constraints. A quality *C* was assigned to horizons that do not show a convincing cor-
 199 relation between observed and predicted data, usually due to data with low signal-to-
 200 noise levels. Stations above the forearc lowlands for which the characteristic slab signa-
 201 ture (Fig. 2b) is decisively absent and where the onset of eclogitization is expected, were
 202 marked with a quality *X*. The nominal depth uncertainty was estimated from the scat-
 203 ter of the local minima in the vicinity of the preferred minimum as determined in the
 204 global search (Fig. 3c).

205 2.3 Fitting of interfaces

206 In total, 171, 143 and 137 quality *A* nodes were determined to constrain the *t*, *c*
 207 and *m* interfaces, respectively. At the trench, 105 nodes at 3 km below the local bathymetry
 208 were inserted to constrain the *t* and *c* interfaces, and at 6.5 km deeper to constrain the
 209 *m* interface, representing typical sediment and igneous crustal thicknesses (Han et al.,
 210 2016). A spline surface (Sandwell, 1987) was fit to these nodes to yield margin-wide depth
 211 models. The spline coefficients were found using singular value decomposition (Wessel
 212 & Becker, 2008; Aster et al., 2018), with the nominal depth uncertainties supplied as weights.
 213 The solution was damped by retaining the 116, 117, and 116 largest singular values for
 214 the *t*, *c* and *m* interfaces, respectively, based on analysis of L-curves and the Akaike in-
 215 formation criterion (Fig. S1).

216 3 Results

217 3.1 Margin-scale slab morphology

218 The signature of subduction stratigraphy can be traced along the forearc from Brooks
 219 Peninsula on northern Vancouver Island, across Vancouver Island, Olympic Peninsula,
 220 the Willamette Valley of Washington and Oregon to Cape Mendocino and into Klamath

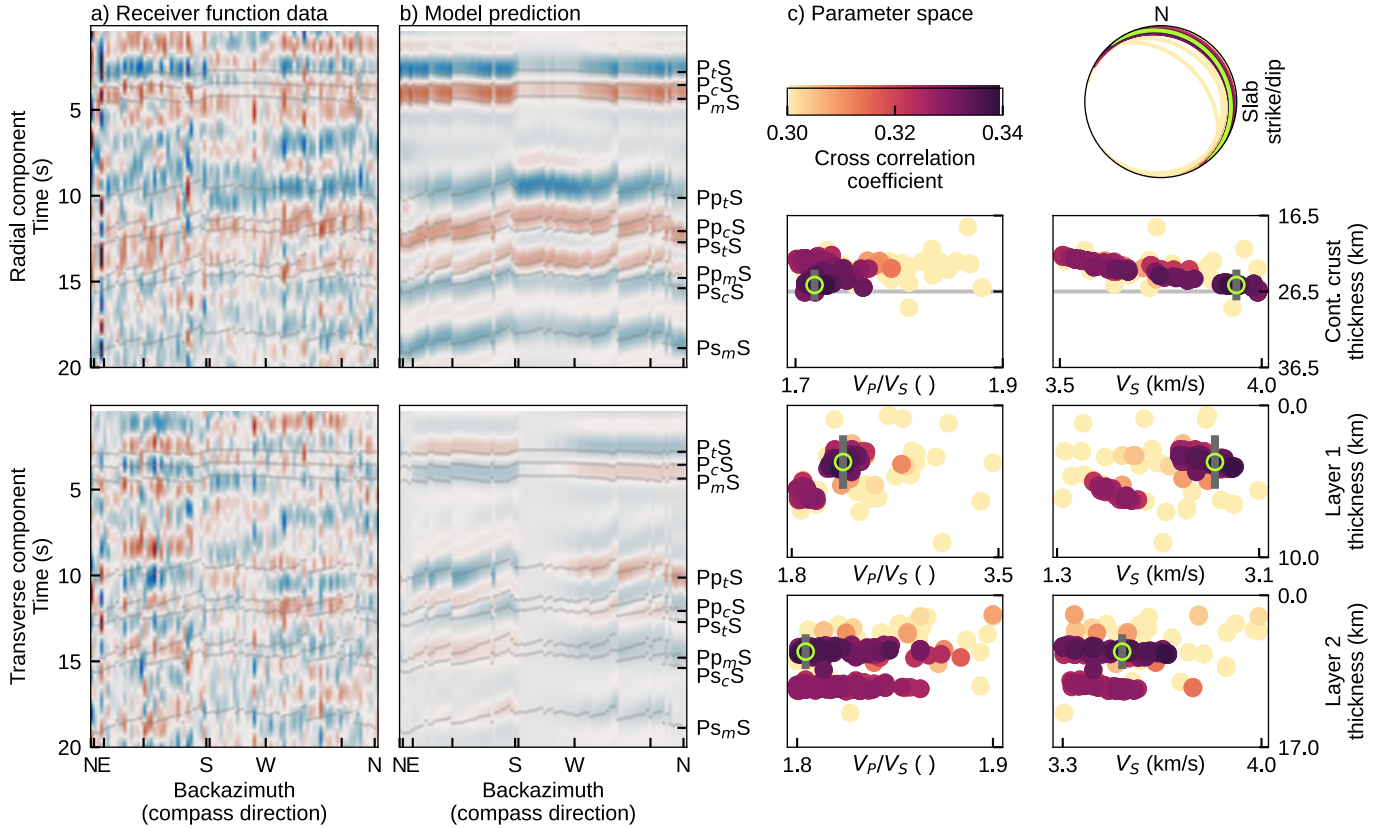


Figure 3. Global search for subsurface parameters. (a) Receiver function data for station C8.TWBB. (b) Predicted data from the best fitting model with phase labels as in Figure 2b. (c) Local minima encountered in the global search for the 11 subsurface parameters (thickness against V_P/V_S in the left column and against V_S in the right column) using a simulated annealing scheme with preferred solution marked with a green circle and nominal depth uncertainties with a gray bar. Note the presence of a local minimum. If such minimum proved more consistent with external constraints and neighboring stations, the global search was repeated within bounds around that minimum.

221 Mountains in northern California (Figs. S2-S50). Recovered velocities of the three model
 222 layers are consistent for neighboring stations (Fig. S51). Slab morphology suggests a di-
 223 vision into four segments: the Klamath, Central, Olympic and Vancouver Island segments
 224 (Fig. 4).

225 The Central segment, between 44° N and 47° N, reveals the steepest dip, between
 226 10 and 20° , and overall deepest slab, with the t horizon located between 15 and 25 km
 227 depth along the coast and dipping to 35 to 45 km depth before losing expression in ad-
 228 vance of the volcanic arc. The Central segment is flanked to the north and south by flat-
 229 ter segments. In the south, the Klamath Segment, located between $\sim 40^\circ$ N and 44° N,
 230 displays a more shallowly dipping slab, a contorted t horizon beneath Cape Mendocino
 231 and a contorted m horizon along the landward projection of the Blanco Fracture zone.
 232 The Olympic Segment, located between 47° N and 49° N, exhibits a shallow dipping (0-
 233 5°) slab beneath the coastal region, and is delimited to the south by steep downward bend
 234 in the t and m horizons near Gray's Harbour and by a bend in slab strike just north of

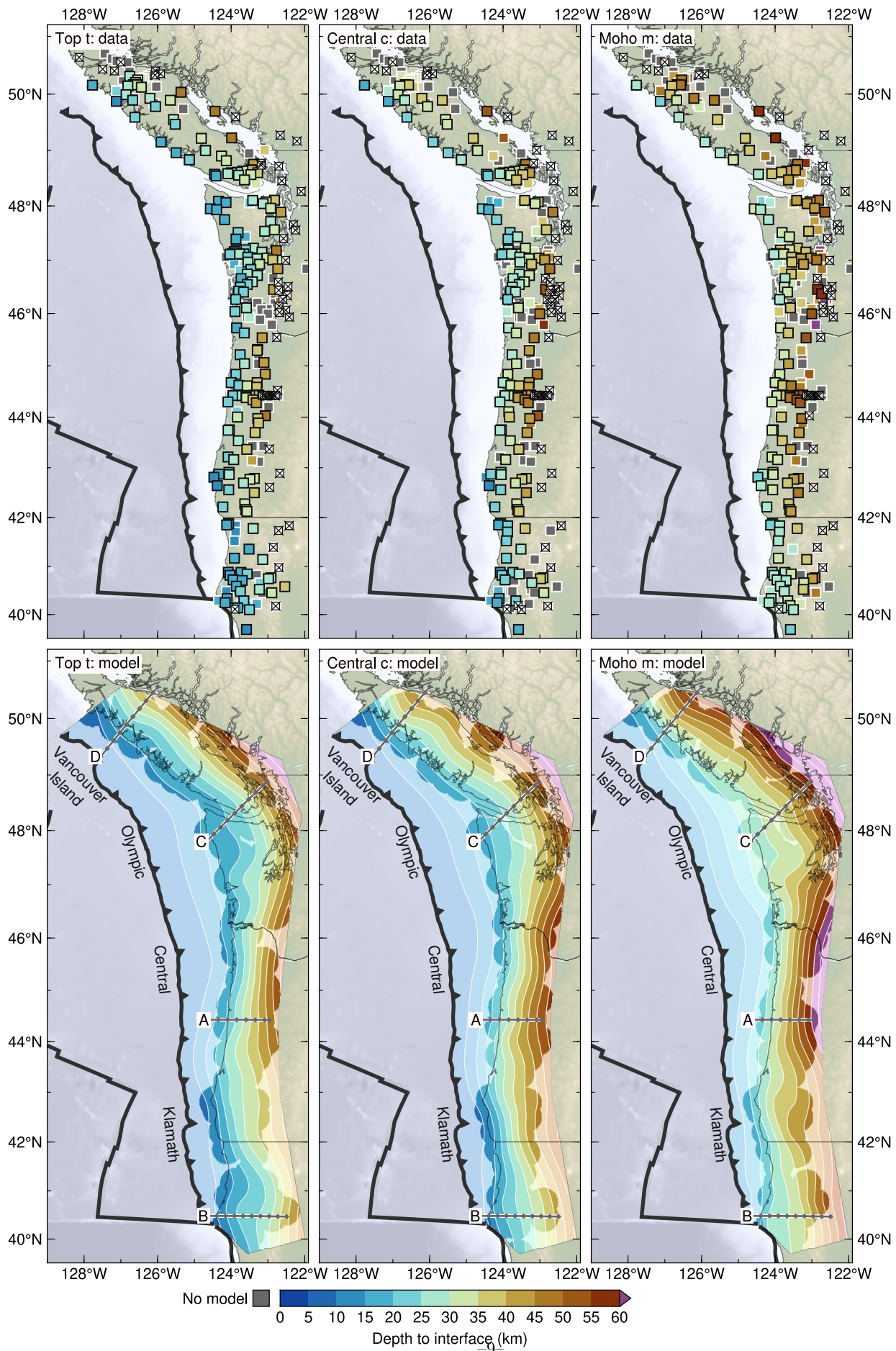


Figure 4. Depth to the t , c and m horizons. Top row: Data points by quality (black frames: A ; white frames: B ; not used for fitting the interface; grayed out: C). Stations marked X do not show the respective interface and are interpreted as the location of the eclogitization front. Bottom row: modeled interfaces (Section 2.3) and profile locations (Figs. 5–8)

235 the Juan de Fuca Strait. Along dip, the slab steepens as it approaches Puget Sound, where
 236 it begins to lose expression (Abers et al., 2009). The northernmost Vancouver Island seg-
 237 ment is characterized by a moderately dipping slab. Near the northern terminus of sub-
 238 duction, north of Nootka Island, the t and c conversions appear disturbed. In summary,
 239 from north to south, the slab (i) dips gently and steepens down dip under Vancouver Is-
 240 land, (ii) dips shallowly beneath the Olympic Peninsula, (iii) steepens significantly be-
 241 neath the Oregon Coastal Mountains, (iv) subducts in a step-like fashion in front of Kla-
 242 math Mountains, and (v) becomes contorted in the Cape Mendocino area. A compar-
 243 ison with previous slab models is shown in Figure S52.

244 3.2 Regional scale

245 3.2.1 Central segment

246 Across the Central segment, the slab has been imaged with seismological methods
 247 using data from the CASC’93 experiment that comprised a temporary broadband ar-
 248 ray of ~ 30 stations deployed across the Oregon forearc (Nabelek et al., 1993). It yielded
 249 the first dense receiver function studies targeting subduction zone structure that clearly
 250 revealed subducting oceanic crust (Rondenay et al., 2001; Bostock et al., 2002; Tauzin
 251 et al., 2016). The comparison of our model with the teleseismic full-waveform tomogram
 252 of Kan et al. (2023) yields a consistent picture of the subduction stratigraphy (Fig. 5).
 253 As in previous studies, Kan et al. (2023) image the subducting Juan de Fuca plate as
 254 a distinctive low- V_S zone, which attains velocities as low as 3.3 km s^{-1} . All three hori-
 255 zons parallel this structure, with t marking the top of the LVZ and c and m marking
 256 two steps in the gradual increase towards high V_S , characteristic for oceanic mantle of
 257 the order of 4.3 km s^{-1} . This structure has a very clear and characteristic expression in
 258 the receiver functions, which weakens near station XZ.A18, beneath the Willamette Val-
 259 ley, as in the tomogram. The entire stratigraphic (t , c , m) sequence brackets weak slab-
 260 related seismicity in the offshore area (Morton et al., 2023). It has a thickness of about
 261 7 km near the coast and thickens arc-ward to about 13 km, with the two layers possess-
 262 ing comparable thickness.

263 3.2.2 Klamath segment

264 Beneath the Mendocino region, the subduction stratigraphy has been imaged as
 265 a moderately high- V_P/V_S zone (1.8-1.9; Guo et al., 2021) complemented by relatively
 266 abundant intraslab seismicity defining a tightly confined Wadati-Benioff zone (e.g., Wang
 267 & Rogers, 1994; Waldhauser, 2009, Fig. 6). The t and m horizons encapsulate the seis-
 268 mically active, moderately high- V_P/V_S zone, with the m horizon falling in good agree-
 269 ment with the $V_P/V_S = 1.7$ contour. Where it projects beneath the Franciscan terrane,
 270 the high- V_P/V_S -zone loses expression and the density of earthquakes diminishes (60 km
 271 from coast in Fig. 6a). Our slab model here indicates a generally shallower dip that steep-
 272 ens again under the Klamath terrane (100 km from the coast), where it indicates that
 273 a low- V_P/V_S anomaly is located within the subduction stratigraphy. Layer 1 is absent
 274 between the coast and the Franciscan terrane and attains a thickness of a few kilome-
 275 ters farther landward. Notably, no seismicity locates within Layer 1. The c horizon defin-
 276 ing the base of Layer 1 approximately aligns with the location of LFEs (Plourde et al.,
 277 2015). The entire subduction stratigraphy has a fairly uniform thickness of 10 km. The

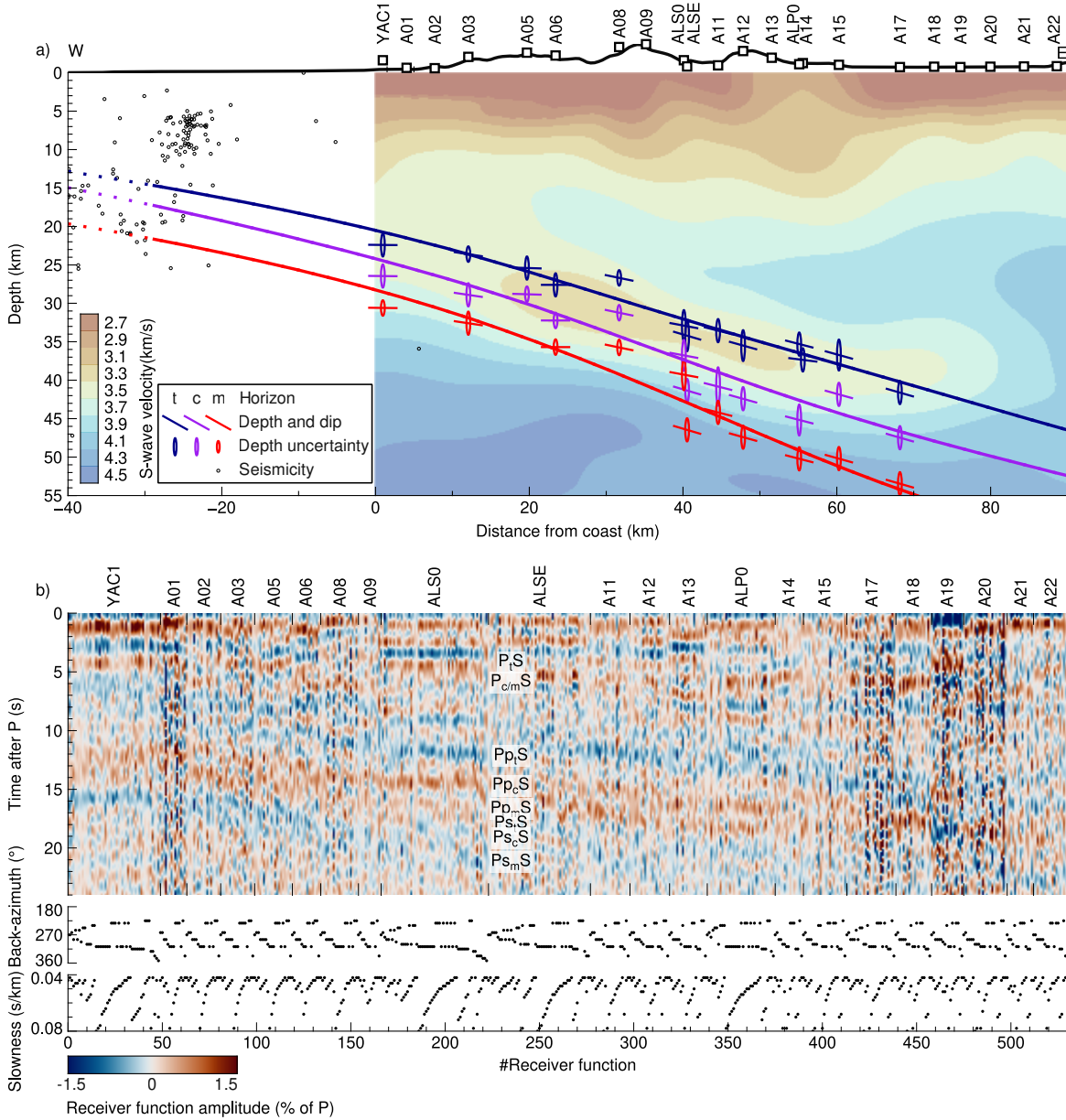


Figure 5. a) Profile A (Fig. 4) with slab model and control points superimposed on the V_S model of Kan et al. (2023) with seismicity from Morton et al. (2023). Comparison with the V_P/V_S image is shown in Fig. S53. b) Receiver function sections of individual stations sorted along the profile, with receiver function within each section sorted by angular distance of the ray back-azimuth from profile azimuth (90°). 1.5–20 s bandpass filter applied. Phase labels correspond as in Fig. 2.

278 receiver function slab signature is difficult to correlate laterally, due presumably to some
 279 combination of variation in overburden and slab properties (Fig. 6b).

280 *3.2.3 Olympic segment*

281 A profile along dip from the western end of the Olympic Peninsula, across the Juan
 282 de Fuca Strait, southern Vancouver Island, and into the Strait of Georgia reveals a flat
 283 lying slab beneath Olympic Peninsula that continues under the Juan de Fuca Strait and
 284 gradually steepens under southern Vancouver Island (Fig. 7a). The t and m horizons
 285 encompass the moderately high- V_P/V_S zones previously interpreted as the subducting
 286 crust in local seismic tomograms (Merrill et al., 2020; Savard et al., 2018). Under the
 287 Olympic Peninsula, this zone is seismically active and m agrees well with the $V_P/V_S =$
 288 1.7 contour. Beneath southern Vancouver Island, m bounds the top of seismic activity
 289 previously interpreted to occur within the subducting mantle (Savard et al., 2018). Layer
 290 1 is absent or very thin beneath the Olympic Peninsula and attains a thickness of about
 291 5 km beneath southern Vancouver Island, where it is aseismic. The c horizon is located
 292 2-3 km above a prominent band of LFE locations (Savard et al., 2018; Armbruster et al.,
 293 2014). Tremor hypocenters from Bombardier et al. (2023, see also Kao et al. (2005)) scat-
 294 ter within and above the subduction stratigraphy. The complex overburden structure
 295 of the Olympic Peninsula hampers a clear identification of c and m ; however, correla-
 296 tions of seismic phases along strike and along dip yield a laterally coherent picture. Be-
 297 neath southern Vancouver Island, the slab reveals a clear and simple receiver function
 298 signature that can be traced beneath the Gulf Islands in the Strait of Georgia and loses
 299 expression toward the British Columbia Lower Mainland (Fig. 7b)

300 *3.2.4 Vancouver Island segment*

301 The Vancouver Island segment exhibits t and m horizons that bracket NE-dipping
 302 regions of elevated V_P/V_S evident in local seismic tomograms. The m horizon coincides
 303 with the $V_P/V_S = 1.7$ contour, that also bounds the top of seismicity which has been
 304 inferred to reside in the oceanic mantle (Figs. 8a and S3–S16; Savard et al., 2018; Mer-
 305 rill et al., 2022). c can best be seen as a pronounced and distinct horizon in southern
 306 and south-central Vancouver Island, where it lies 2-4 km underneath t and decisively above
 307 LFE locations (Savard et al., 2018).

308 Towards north-central Vancouver Island, the subduction stratigraphy appears to
 309 thicken substantially downdip, from ~ 8 km near the coast, to ~ 16 km inland. Layer 1
 310 and Layer 2 contribute in equal part to the combined thickness. The c horizon gener-
 311 ally follows the LFE locations (Savard et al., 2020). Substantial scatter in the station
 312 measurements and difficulties in reconciling phase correlations across closely spaced sta-
 313 tions attest to the complex subsurface structures that are also evident in local seismic
 314 tomography and may be related to subduction of the Nootka Fault Zone as the north-
 315 ern terminus of JdF subduction (Fig. 8b; Savard et al., 2018; Merrill et al., 2022).

316 **4 Interpretation of the subduction stratigraphy**

317 The combined thickness of the stratigraphic package comprising t , c , m horizons
 318 exceeds almost everywhere the nominal thickness of the incoming oceanic crust of ~ 6.5 km
 319 by 2 to 12 km (Fig. 9a). A thickness of ~ 7 km is only resolved along the southern Cen-
 320 tral segment, between ~ 43 and 44° N. Model regularization may dampen slab complex-
 321 ity and smooth over interface steps on a ~ 20 km scale (e.g., m in Fig. 6a), but the ex-
 322 cessive thickness of the slab stratigraphy is a robust feature of the model and is almost
 323 always underpinned by individual point station measurements. Additional material, other
 324 than actively subducting igneous oceanic crust, must therefore make up the subduction
 325 stratigraphy.

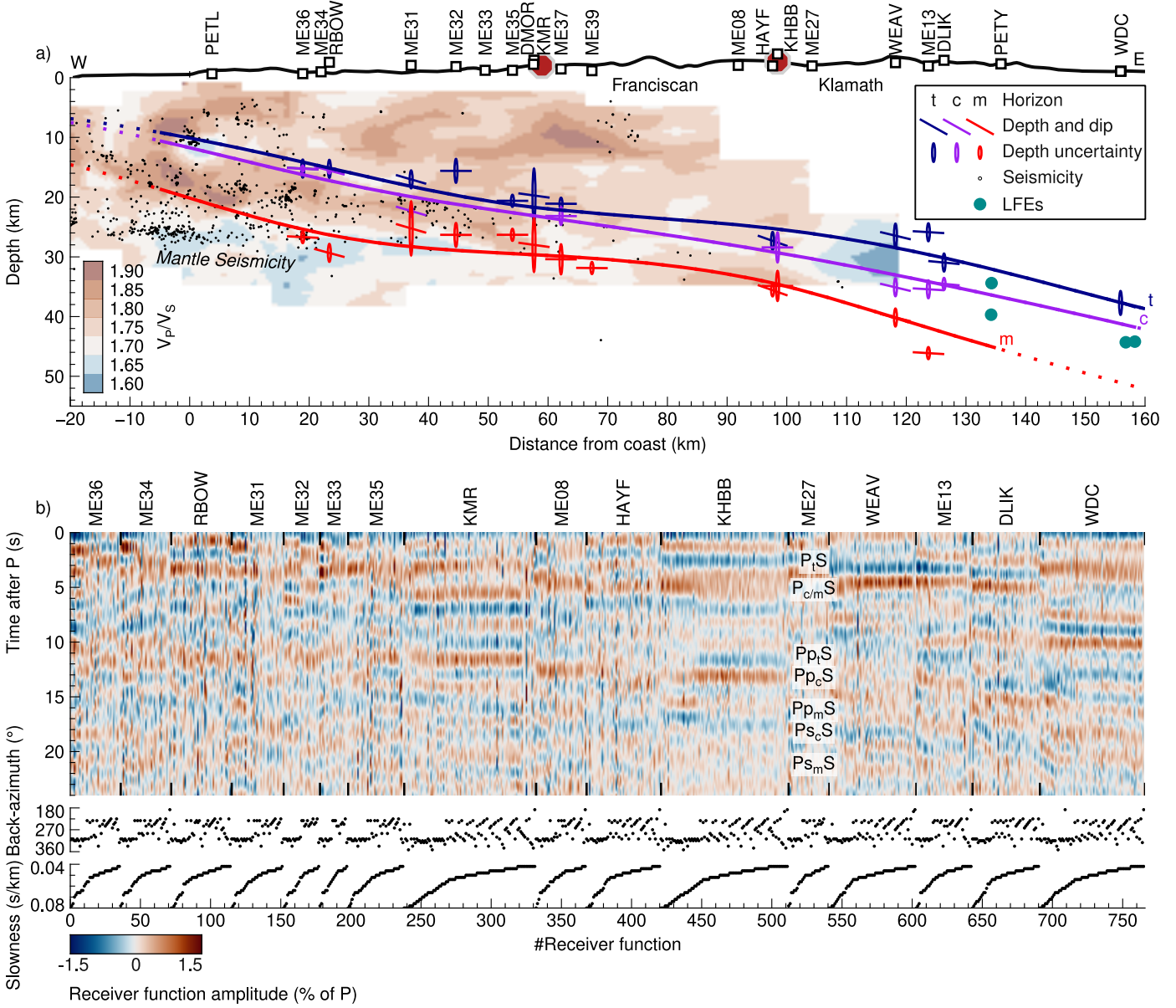


Figure 6. As Figure 5, but for Cape Mendocino profile B (see Fig. 4). Tomogram and seismicity from Guo et al. (2021), LFEs from Plourde et al. (2015). A comparison with the V_S image is presented in Figure S54. Receiver functions filtered between 2 and 20 s.

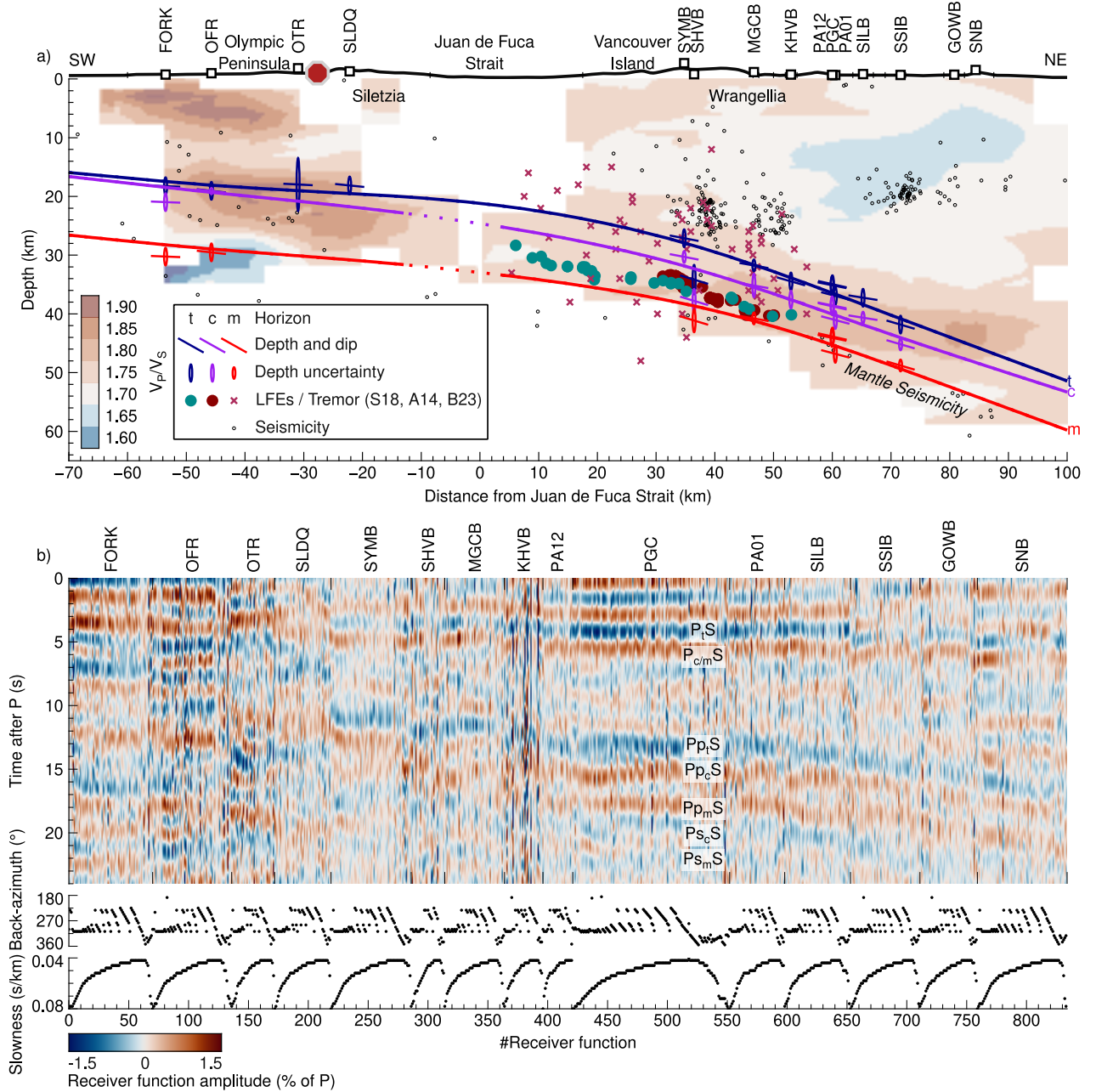


Figure 7. As Figure 5 for profile C across Olympic Peninsula (negative profile distances) and Southern Vancouver Island (positive profile distances). Tomograms and seismicity from Merrill et al. (2020) (Olympic Peninsula) and Savard et al. (2018) (Vancouver Island). LFE and tremor locations are from: (A14, brown dots) Armbruster et al. (2014); (S18, cyan dots) Savard et al. (2018); (B23, purple crosses) Bombardier et al. (2023). Comparison with V_S shown in Figure S55. Receiver functions filtered between 2 and 20s.

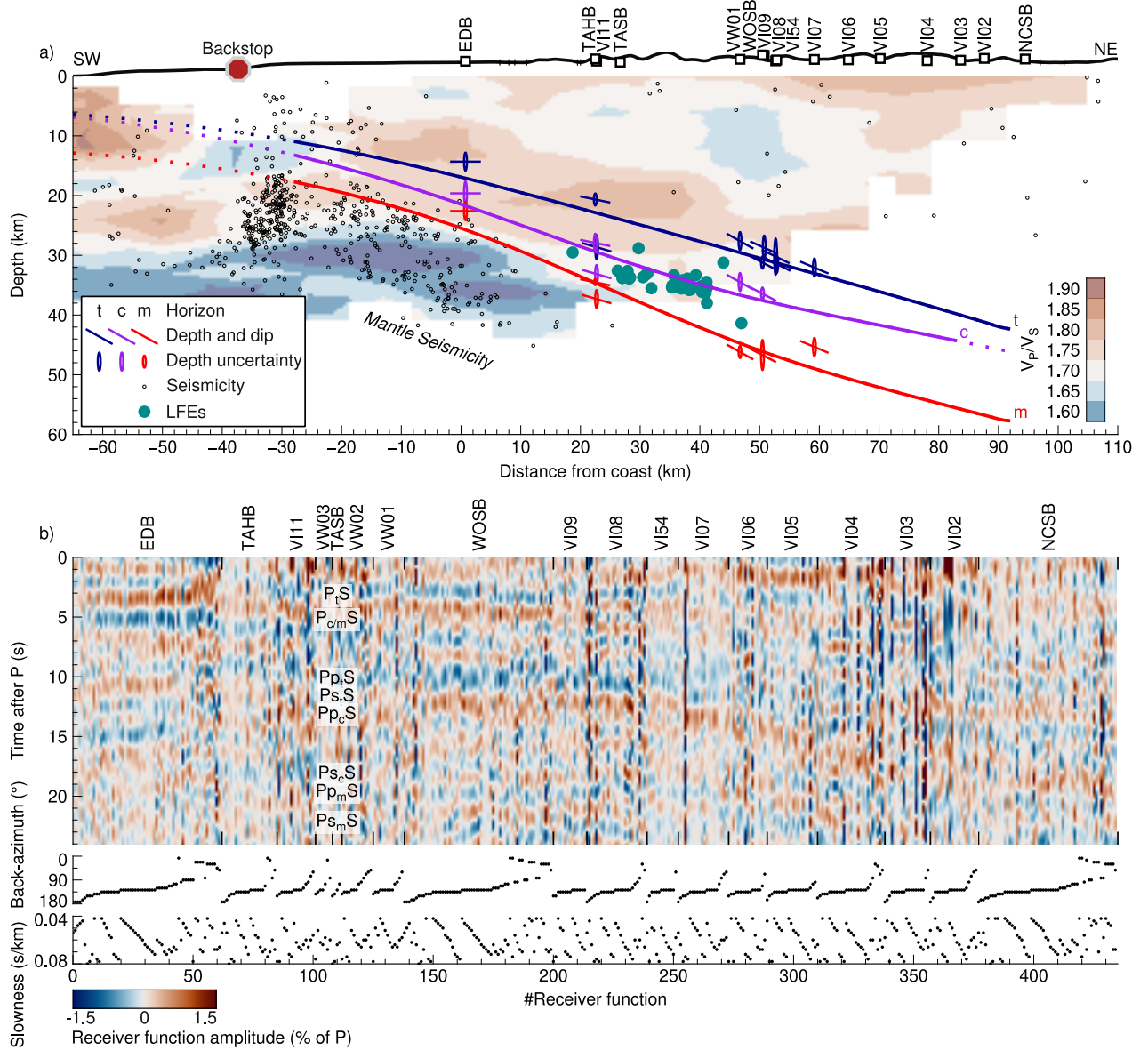


Figure 8. As Figure 5, but for profile D across Northern Vancouver Island. Tomogram and seismicity from Merrill et al. (2022). LFE locations from Savard et al. (2020). Comparison with V_S shown in Figure S56. receiver functions filtered between 2 and 20 s.

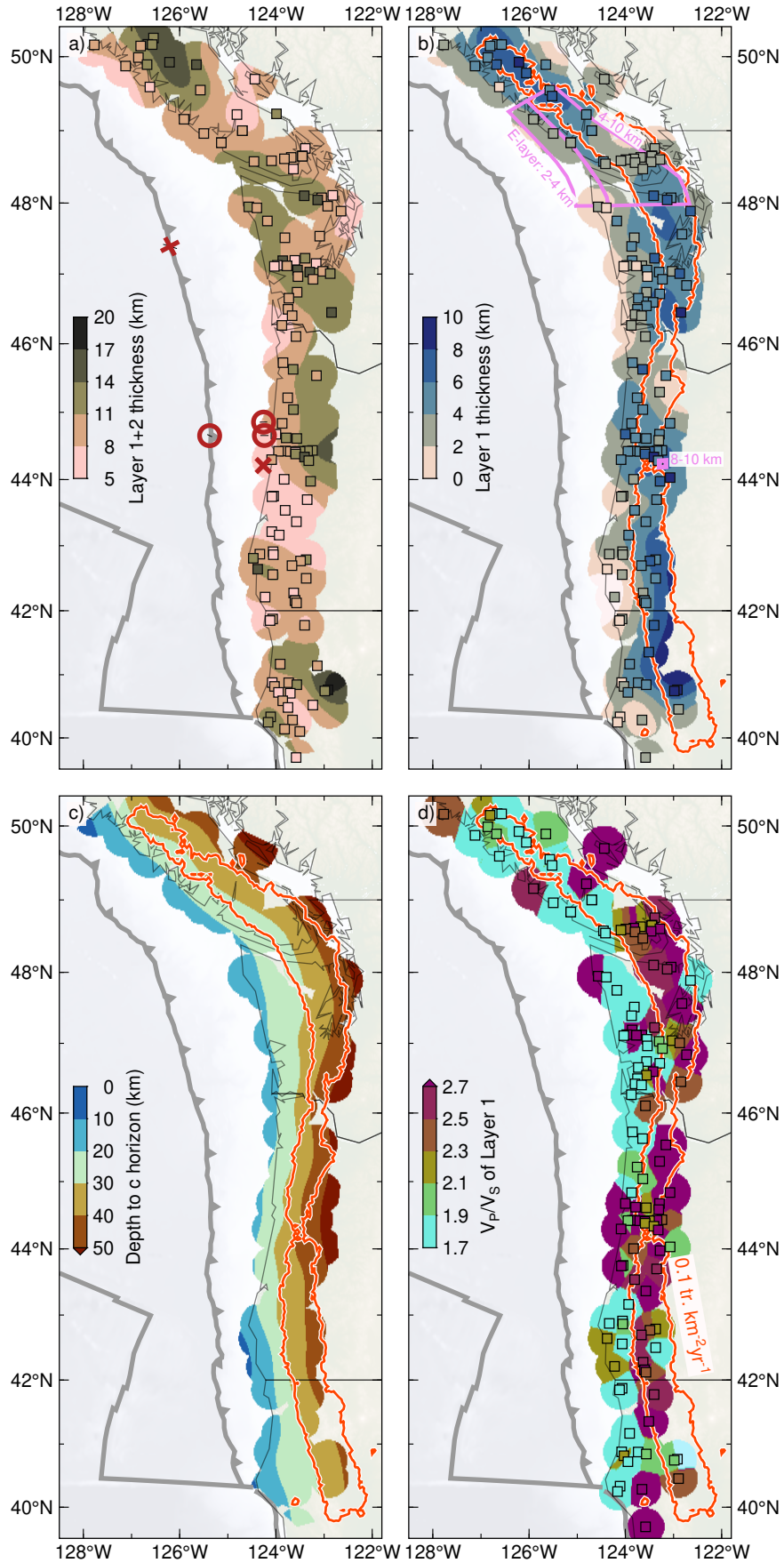


Figure 9. Select properties of slab stratigraphy. a) Combined Layers 1 and 2 (t -to- m) thickness. 'O' marks places where sediment subduction has been detected on marine seismic surveys, 'X' where sediment subduction is absent (Han et al., 2016; Tréhu et al., 2012). The thickness of the subduction stratigraphy exceeds the thickness of the igneous oceanic crust. b) Layer 1 (t -to- c) thickness and tremor zone (Wech, 2010). Downdip thickening of Layer 1 correlates with tremor locations. c) Depth to c horizon correlates closely with tremor occurrence (Fig. 10c and d). d) V_P/V_S of Layer 1.

326 Layer 2 and the underlying mantle half-space, separated at m , were designed to cor-
 327 respond to igneous oceanic crust and pristine mantle. Where seismic velocities and seis-
 328 micity images are available, the model appears to have captured this contrast appropri-
 329 ately, so that we confidently interpret m as the oceanic Moho. We cannot exclude the
 330 possibility that, where the plate is hydrated, m is biased into the oceanic mantle, ly-
 331 ing deeper than the Moho. Signs of mantle hydration may be present under the Cape
 332 Mendocino coast and offshore northern Vancouver Island, suggested by a diffuse tomo-
 333 graphic Moho, abundant mantle seismicity and the subduction of major fracture zones
 334 (Figs. 6 and 8, e.g., Wilson, 1989; Chaytor et al., 2004; Rohr et al., 2018; Merrill et al.,
 335 2022). Such signatures are, however, not universally present.

336 The excess thickness is more likely developed above the plane of active subduction,
 337 that is, in Layer 1. Where the thickness of Layer 1 is substantial (i.e., from t to c ; Fig. 9b),
 338 the E-layer (or a reflective zone above the slab) has been detected in reflection seismic
 339 surveys (Fig. 9b; Clowes, Brandon, et al., 1987; Nedimović et al., 2003; Keach et al., 1989;
 340 Tréhu et al., 1994). Nedimović et al. (2003) suggest that emergence of the E-layer is re-
 341 lated to the occurrence of episodic tremor and slip. The E-layer is typically thicker than
 342 Layer 1, which suggests that Layer 1 is part of the E-layer (Calvert et al., 2020). Within
 343 the tremor zone, defined by the $0.1 \text{ tremor yr}^{-1} \text{ km}^{-2}$ contour (Fig. 9b-d; downloaded from
 344 <https://pnsn.org>; Wech, 2010), the mean and median V_P/V_S in Layer 1 are 2.49 ± 0.14
 345 (2σ) and 2.44. Outside the tremor zone V_P/V_S is lower, with a mean value of 2.28 ± 0.14
 346 and median value of 1.95 (Figs. 9b, 10a and b). A two-sample Kolmogorov-Smirnov test
 347 yields a p -value of $5 \cdot 10^{-5}$, indicating that the distribution of V_P/V_S values of Layer 1
 348 from inside and outside the tremor zone are statistically different with $>99\%$ confidence.
 349 This suggests that the development of Layer 1 as a high- V_P/V_S ULVZ is related to tremor,
 350 in agreement with previous findings (Audet et al., 2009; Song et al., 2009). We interpret
 351 t in the tremor zone as the top of this ULVZ. Projecting the tremor epicenters (Wech,
 352 2010) onto the t and c horizons yields tremor depth of $32 \pm 10.8 \text{ km}$ and $38 \pm 10.2 \text{ km}$
 353 (2σ), respectively (Fig. 10c and d). Tremor depth are concentrated more tightly when
 354 projected to the c horizon, suggesting tremor occurs closer to the base of Layer 1 (Fig. 9c).
 355 Inside the tremor zone, where Layer 1 corresponds to the ULVZ, c marks a stark ma-
 356 terial contrast against the underlying oceanic crust and we interpret c as the base of the
 357 ULVZ.

358 Between the coast and the tremor zone, except between 44 and 45° N , Layer 1 is
 359 typically thinner (Fig. 9b) and its V_P/V_S is lower (Figs. 9d and 10b), attaining normal
 360 values for basaltic material (~ 1.8). Layers 1 and 2 still exhibit a combined thickness in
 361 excess of the incoming oceanic crust with Layer 1 displaying properties that are, nev-
 362 ertheless, similar to oceanic crust. The t horizon is here the top of this excess volume.
 363 The c horizon here usually marks a less prominent material contrast than inside the tremor
 364 zone. It may seem natural to interpret c as the base of a possible sedimentary blanket
 365 above an underlying igneous oceanic crust (e.g., Delph et al., 2018), but we note here
 366 that Layer 2 is frequently thicker than oceanic crust, hence the interpretation of c as the
 367 base of sediments is possible, but not universal. Horizon c may alternatively represent

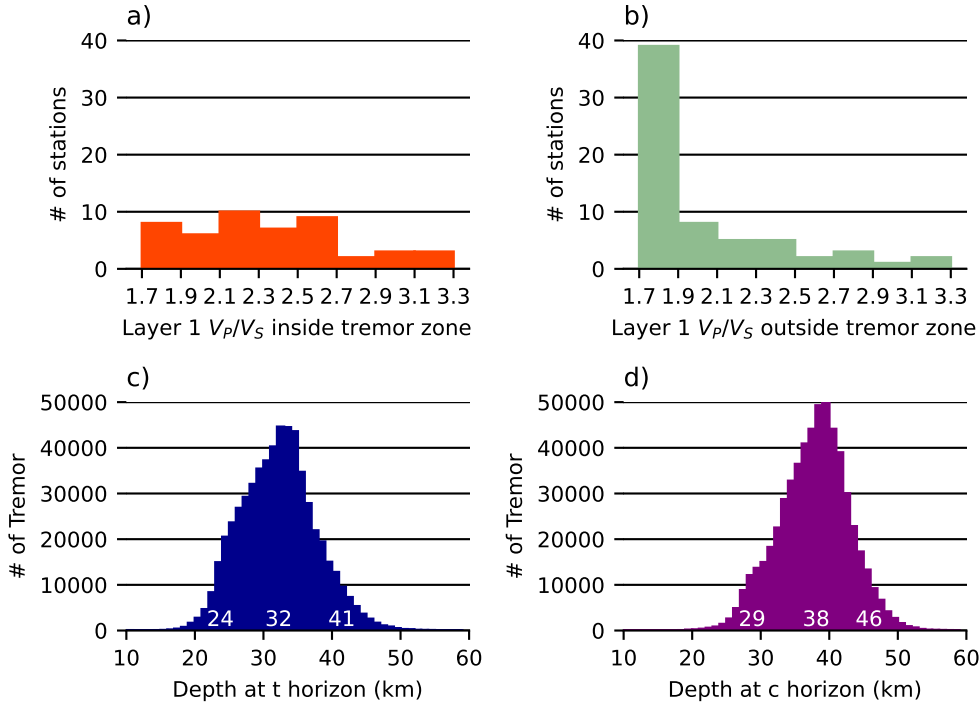


Figure 10. Properties of Layer 1 in relation to tremor. (a and b) V_P/V_S of Layer 1 at stations (a) inside and (b) outside the tremor zone ($0.1 \text{ tremor km}^{-2}\text{yr}^{-1}$ contour; Fig. 9). (c and d) Depth distribution of tremor epicenters projected onto the (c) t and (d) c horizons. Numbers at the base indicate the 5%, 50% and 95% quantiles of the depth distribution.

368 a velocity gradient within a sedimentary layer or the base of altered material belonging
 369 to overriding continental crust.

370 5 Discussion

371 5.1 Possible controls on slab morphology

372 The overall slab morphology exhibits a first-order correlation with the location of
 373 the static backstops in the Cascadia subduction system (Fig. 11; Watt & Brothers, 2020).
 374 These are kinematic discontinuities that are related to distinct strength contrasts within
 375 the continental crust formed by accreted crystalline terranes. The most important ter-
 376 rane is Siletzia, a basaltic large igneous province that formed offshore as on oceanic plateau,
 377 possibly related to magmatism of the Yellowstone hotspot. It can be mapped along coastal
 378 Oregon, Washington and British Columbia (Wells et al., 2014). An associated aeromag-
 379 netic anomaly indicates that Siletzia is most voluminous under central and northern Ore-
 380 gon (Wells et al., 1998). Reflection seismic together with wide-angle seismic data
 381 and geomorphologic markers reveal that the base of Siletzia is up to 35 km deep and pos-
 382 sibly extends down to the plate interface (Tréhu et al., 1994). This inference is substan-
 383 tiated by magneto-telluric data that image a voluminous resistive body, interpreted as
 384 representing Siletzia, that meets the plate interface in coastal Oregon (Egbert et al., 2022).
 385 Kinematically, the thickened Siletz terrane forms a distinct block that rotates clockwise
 386 with respect to stable North America (Wells et al., 1998) and displays the lowest inter-
 387 seismic vertical uplift rates along the entire forearc (Mitchell et al., 1994). Where the

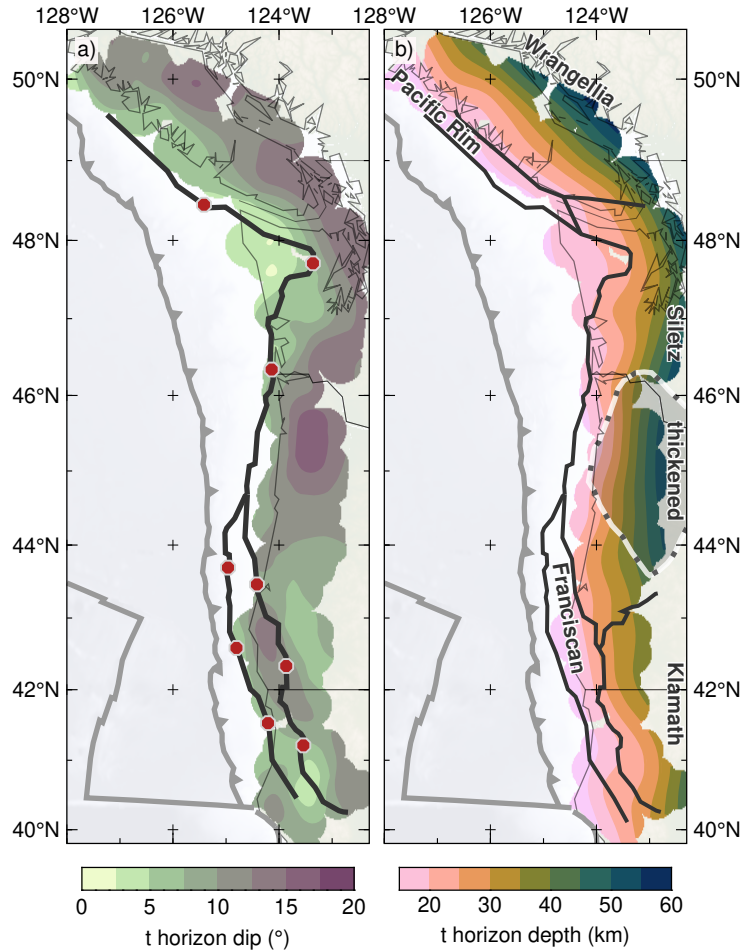


Figure 11. Dip (a) and depth (b) of the t horizon. Static backstop (line with red octagons in a) and terrane boundaries (thick lines in b) modified after Watt & Brothers (2020). Shaded area enclosed by white dashed line represents thickened Siletz terrane detected in aeromagnetic data (after Wells et al., 1998). The location of the terrane backstop correlates with and may exert a first order control on slab morphology.

388 Siletz terrane recedes far inland on the eastern side of Olympic Peninsula, giving way
 389 to the Olympic complex formed by underthrust marine sediments (e.g., Brandon & Calder-
 390 wood, 1990), the slab lies shallower and flatter than anywhere else along the entire on-
 391 shore forearc. Conversely, where the western boundary of the Siletz terrane is located
 392 off-shore and Siletzia is thickest, the slab is deepest and has its steepest dip (Fig. 11).
 393 This suggests that the competence and rigidity of the Siletz block forces the descent of
 394 the Juan de Fuca slab. It has been suggested that the Kumano pluton influences the sub-
 395 ducting Philippine Sea Plate in a similar manner below southwest Japan (Arnulf et al.,
 396 2022).

397 In between the shallowly dipping Olympic and steeply dipping Central segments,
 398 a pronounced southward downward bend in the slab is evident along a line extending
 399 between Gray's Harbour and the southern end of Puget Sound. The bend is evident
 400 in the raw receiver functions, where the timing of the P_mS conversion increases, e.g., from
 401 ~ 3 to ~ 4 s for rays arriving from NNW relative to those arriving from SSE azimuths at
 402 station US.NLWA and again from 4 s to 4.5 s just south of that at station UW.WISH (Fig. 12).

Perhaps significantly, the three largest intermediate depth earthquakes in Cascadia, the 1949 $M6.7$ Olympia (Nuttli, 1952), 1965 $M6.7$ Puget Sound (Langston & Blum, 1977) and 2001 $M6.8$ (Ichinose et al., 2004; Kao et al., 2008) earthquakes occurred near the down-dip continuation of this bend, at depths at or immediately below those projected for the oceanic Moho.

Along the Klamath segment to the south (south of 44°N), slab structure is complex. The Gorda Plate, a relatively young and highly deformed plate (Wilson, 1989; Chaytor et al., 2004), encounters two static backstops, namely the western boundaries of the Franciscan complex and the Klamath terrane (Fig. 11; Clarke, 1992; Watt & Brothers, 2020), and is bounded to the south by the Mendocino Fracture zone. The southern and eastward trending seaward boundary of the thickened Siletz terrane has a reduced impact on slab morphology, resulting in the southward transition to a more gently dipping slab (Fig. 11). This geometry is interrupted with emergence of the Klamath terrane, where the steepest dip of the slab is located near the coast, bending behind the first, seaward backstop, and unbending beneath the second, landward, backstop. In the Cape Mendocino area the slab top is contorted in a fashion that yields a flat-lying segment just behind the coast. Because of the generally lower dip in advance of the volcanic arc and its unbending beneath the southern Siletz and Klamath terranes, it appears as if the Gorda plate does not subduct as readily as the Juan de Fuca plate. A possible cause for this behaviour is an increased buoyancy of the youngest subducting lithosphere (5-6 Ma at the trench, e.g., Wilson, 1993)

5.2 Excess thickness of Subduction Stratigraphy

The nature and origin of the E-layer as a prominent element of the subduction zone stratigraphy that emerges abruptly along the dip trajectory in the vicinity of southern Vancouver Island is a long standing conundrum in the understanding of the Cascadia subduction zone (e.g., Calvert et al., 2020; Calvert, 1996; Calvert et al., 2011; Nedimović et al., 2003; Clowes, Brandon, et al., 1987). Our data show a qualitative correlation between a thick Layer 1 and a thick (>4 km) E-layer where the latter has been imaged (Fig. 9b). We also suggest that the reflective zone mapped by COCORP in central Oregon (Fig. 9b; Keach et al., 1989) may manifest the presence of a structure with similar origin since it also coincides with a thick Layer 1. Assuming this association holds true along the entire margin, our data would suggest that the E-layer is ubiquitous. Its abrupt emergence along dip is likewise reflected in our data: Coastal stations have a tendency to exhibit a thin or absent Layer 1, whereas inland stations generally possess a thick one (Fig. 9b), consistent with previous inferences of Layer 1 thickening near the coast line from an amphibious receiver function study (Audet & Schaeffer, 2018). Interestingly, the combined (Layer 1 + Layer 2) thickness of the subduction stratigraphy does not obey the same trend. Places of a thin or absent Layer 1 may have an overall thick subduction stratigraphy (e.g., coastal Olympic Peninsula and Cape Mendocino) and a significantly thick Layer 1 may correspond to a subduction stratigraphy that does not much exceed the thickness of the incoming oceanic crust (e.g., ~ 7 km thickness between 43°N and 44°N ; Fig. 13a).

Sediments entering the subduction system may contribute to the subduction stratigraphy (e.g., Delph et al., 2018) but information about the amount of subducting sediment at the time of writing is scarce. Tréhu et al. (2012) interpret sediments subducting beneath Siletzia on two seismic lines near 45°N (circles on Fig. 9a), but not on a third line closer to 44°N , (cross on Fig. 9a). Within the same latitude interval, the characteristic transition from thickened to normal subduction stratigraphy occurs, suggesting that these subducting sediments make up for the extra thickness (Fig. 13b). In contrast, Han et al. (2016) document no sediment subduction at the latitude of the Juan de Fuca Strait, where we image a thick (~ 11 km) subduction stratigraphy. However, it is possible that sediment subduction was occurring at the trench in the latter region at 3 Ma

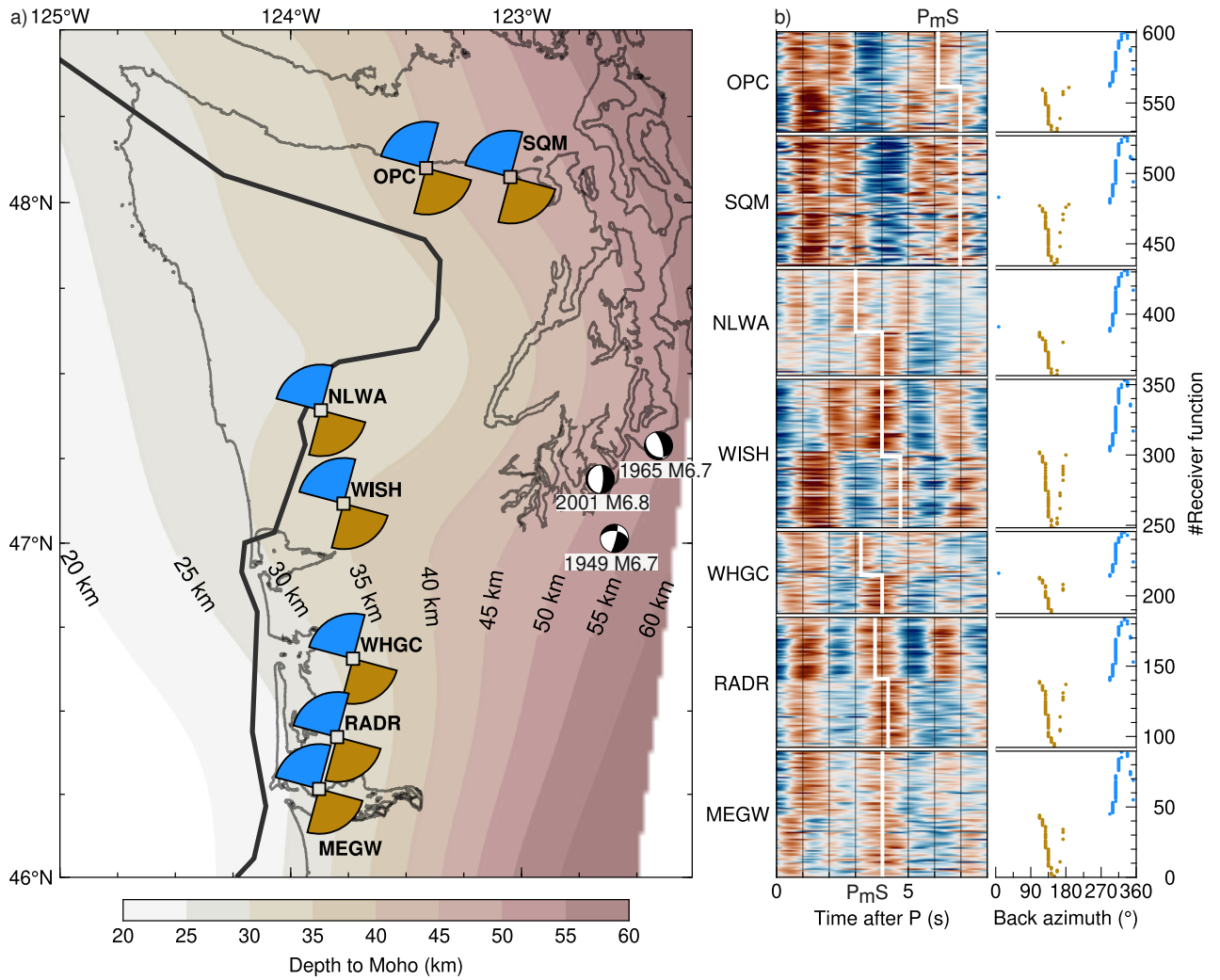


Figure 12. Downwarped Moho from the Olympic Peninsula to Gray’s Harbour. (a) Map view with Moho depth contours as well as locations and receiver function ray back-azimuths of stations shown on the right. Earthquake locations and focal mechanisms from International Seismological Centre (2023). (b) Radial receiver functions sorted by back-azimuth. Rays arriving from NNW colored blue, from SSW coloured gold. Note the southward down Moho-steps (P_mS) at stations coincident with a thickening low velocity zone above at stations NLWA, WISH, WHGC and RADR.

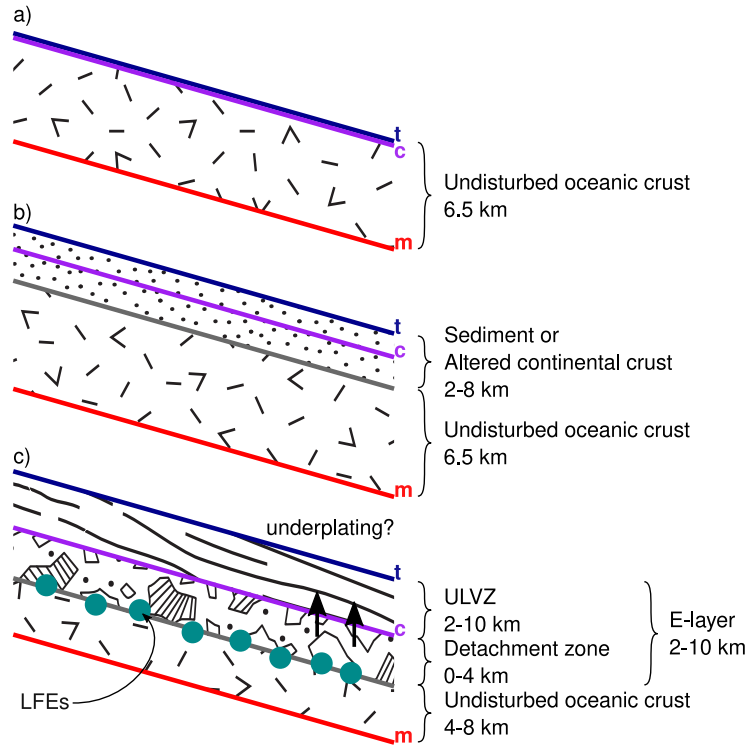


Figure 13. Possible subduction stratigraphies present in the Cascadia subduction zone. (a) Subduction of undisturbed oceanic crust (e.g. Central – South Oregon). (b) Sediment subduction, *c* may represent the base of the sedimentary layer or a horizon within the sediments (e.g. Olympic Peninsula, Northern Oregon). (c) E-layer on top of the subducting crust. LFES locations may indicate a detachment horizon at or below the base of the ULVZ. Low seismic velocities and in-situ thickening above suggest ongoing underplating (e.g. Southern Vancouver Island)

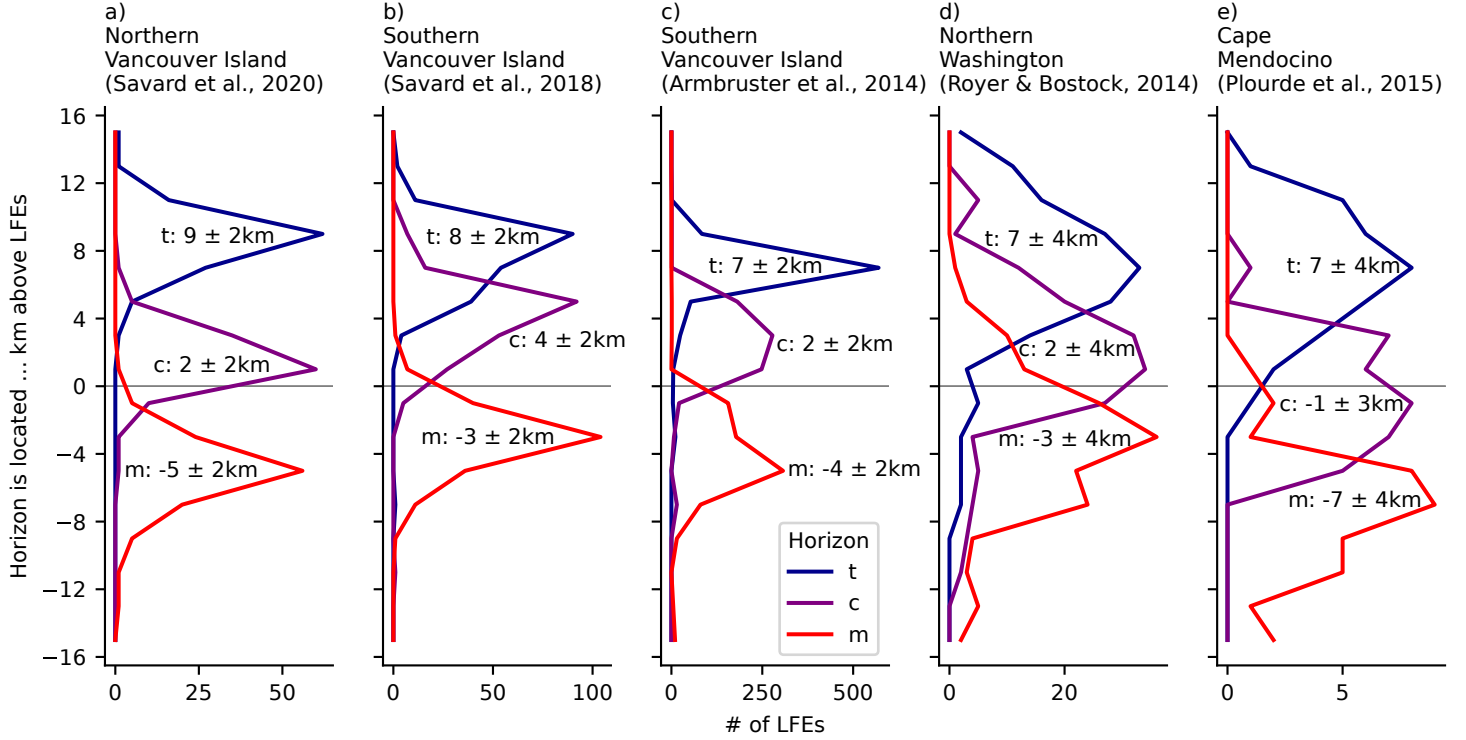


Figure 14. Histograms of the depth of t , c and m horizons relative to LFE locations for different regions. Bin width is 2km. LFEs are most closely located to the c horizon. For Vancouver Island, the data indicate that LFEs occur in Layer 2, between c and m

ago, and subsequently ceased. More data are required to define conclusively where sediment subduction contributes to subduction stratigraphy thickness.

We note that Layer 1 emerges at around 30 km depth and gains thickness along the subduction trajectory, and that this thickness is unrelated to the thickness of the subduction stratigraphy updip of this depth (Figs 9a and b). This observation suggests that Layer 1 thickens in-situ and develops a ULVZ through some depth-activated process. Elevated $V_P/V_S > 2.0$ (Figs 9b and d) suggests that the medium is fractured and saturated with pressurized fluids (Christensen, 1984), implying it has lost structural integrity and strength. As a weak zone, the ULVZ is likely to host slip (e.g., Wech & Creager, 2011; Luo & Liu, 2021). LFE hypocenters are located near the base of the ULVZ (Fig. 14; Calvert et al., 2020), suggesting that the plate boundary is located near c . Excess thickness may be due to underplating of subducting material, either of sediments atop the oceanic crust (e.g., Delph et al., 2018), or of the upper basaltic crust which may lose structural integrity through wear (Fig. 13c, see also e.g., Calvert et al., 2020; Clowes, Brandon, et al., 1987). Moderately high seismic velocities ($V_S > 3.2$ and $V_P/V_S < 1.9$) indicated by our inverse modeling results for Layer 2 (Figs. 2 and S51) preclude the presence of pervasive fracturing and pressurized fluids (Christensen, 1984). Instead, the presence of slivers of oceanic crust, large enough to *not* reduce seismic velocities significantly, would be consistent with LFE occurrence inside Layer 2. The subordinate slip represented by the LFEs during ETS episodes is consistent with the process of initiating detachment of the subducting oceanic crust at the LFE horizon (Fig. 13c). Slow slip, which makes up the main share of the slip budget at depth (Dragert et al., 2001, 2004; Kao et al., 2010; Bostock

476 et al., 2015), may well be located at or above c , that is at the base or inside the 4-10 km
477 thick ULVZ.

478 Subcretion and underplating is consistent with earlier inferences made for the on-
479 shore Cascadia forearc from a wealth of geophysical data. Calvert et al. (2011) interpret
480 underplating of sediments as taking place south of Puget Sound. Calvert (2004) and Clowes,
481 Brandon, et al. (1987) inferred that the E-layer constitutes underplated metabasaltic ma-
482 terial beneath southern Vancouver Island based on high seismic velocities. The corre-
483 spondence between these inferred sites of underplating with the thick ULVZ detected here
484 and the widespread distribution of the ULVZ suggest that underplating is occurring through
485 the majority of the entire Cascadia forearc (e.g., Delph et al., 2021).

486 6 Conclusion

487 Receiver functions provide valuable insights into the subduction of the Juan de Fuca
488 and Gorda plates in the Cascadia region. Based on previous studies of receiver-side for-
489 ward and back-scattered mode conversions, we parameterize subduction stratigraphy in
490 three horizons t , c and m . Mapping these horizons across the forearc reveals flatter slab
491 segments beneath the Olympic Peninsula and Cape Mendocino, central Oregon exhibits
492 a steeply dipping slab. Below most of Vancouver Island the slab is marked by modest
493 dips ($\sim 7\text{--}12^\circ$). This slab morphology appears to be influenced by the mechanical strength
494 and density of accreted crystalline terranes. A notable Moho step south of the Olympic
495 Peninsula may relate to recurrent, large, intermediate-depth earthquakes beneath Puget
496 Sound. In addition, the presence of a thick topmost layer in the subduction stratigra-
497 phy may indicate the widespread occurrence of the E-layer. Previous interpretations sug-
498 gest that the E-layer represents underplated slab material, including both sediments and
499 metabasalt, implying that underplating occurs through most of the Cascadia forearc.

500 Data and Code availability

501 The raw model parameters and slab horizons are part of the supplement of this manuscript
502 and will be made available as a data publication after peer review. The networks with
503 the following FDSN network coded were used in this study: BK (Northern California
504 Earthquake Data Center, 2014), C8, CC (Cascades Volcano Observatory/USGS, 2001),
505 CN (Natural Resources Canada (NRCAN Canada), 1975), IU (Albuquerque Seismolog-
506 ical Laboratory/USGS, 2014), NC (USGS Menlo Park, 1966), PO, TA (IRIS Transportable
507 Array, 2003), UO (University of Oregon, 1990), US (Albuquerque Seismological Labo-
508 ratory (ASL)/USGS, 1990), UW (University of Washington, 1963), X4 (2016–2021; Cakir,
509 2016), XA (2008–2009; Trehu & Williams, 2008), XD (2014–2016; Creager, 2014), XQ
510 (2007–2009; Levander, 2007), XU (2006–2012; Malone et al., 2006), XZ (1993–1994), YS
511 (2001–2003; Brodsky, 2001), YW (2007–2010; Brudzinski & Allen, 2007). Seismic wave-
512 forms are available via the IRIS Data Management Center (IRISDMC; [http://service](http://service.iris.edu/fdsnws/dataselect/1/)
513 [.iris.edu/fdsnws/dataselect/1/](http://service.iris.edu/fdsnws/dataselect/1/)) and/or the Northern California Earthquake Data
514 Center (<https://service.ncedc.org/fdsnws/dataselect/1/>). Receiver functions were pro-
515 cessed with *RfPy* (Audet, 2020). Synthetic receiver functions were computed with *PyRay-*
516 *sum* (Audet & Bloch, 2022). Numerical methods of the global parameter search are from
517 *SciPy* (Virtanen et al., 2020), for signal processing and data manipulation from *NumPy*
518 (Harris et al., 2020). Fitting of the spline surface was done with *greenspline*, which is part
519 of *GenericMappingTools* (Wessel et al., 2019). Maps were drawn with *PyGMT* (Uieda
520 et al., 2023) using the perceptually uniform *Scientific colour maps* (Crameri et al., 2020).
521 Graphs were plotted with *Matplotlib* (Hunter, 2007). Seismic data were handled with
522 *ObsPy* (Krischer et al., 2015).

Acknowledgments

We thank Suzanne Carbotte for generous and substantive discussion and preview of CASIE'21 results. Hao Guo, Jeffrey McGuire, Leo Kan, Sebastien Chevrot, Reid Merrill and Genevieve Savard kindly made their seismic tomograms and relocated seismicity available. Paul Wessel and the *GMT* community supported the computation of regularized spline surfaces. Discussions with Raul Mendoza and Simon Peacock provided valuable insights into Cascadia forearc architecture. Leonardo Colavitti and an anonymous reviewer provided valuable comments that helped to improve the manuscript. This research was funded by Deutsche Forschungsgemeinschaft grant BL 1758/1-1 to WB, and NSERC Discovery grants RGPIN-2021-03039 to MGB and RGPIN-2018-03752 to PA.

This research regards the ancestral homelands and waters of hundreds of diverse and distinct Indigenous Peoples. Among them are the Kwakwaka'wakw Peoples, the Nuu-chah-nulth Peoples, the Makah Peoples, the Coast Salish Peoples, the Quileute Peoples, the Chinookan Peoples, the Siletz People, the Cow Creek Band, the Grand Ronde Community, the Coos, Lower Umpqua, and Siuslaw Peoples, the Klamath Tribes, the Hupa People, the Yurok People, and the Karuk People. It was undertaken at the UBC Vancouver campus on the traditional, ancestral, and unceded territories of the Musqueam People and at the University of Ottawa, located on unceded Algonquin territory. Kayla Lar-Son of UBC's Xwi7xwa Library provided assistance in the formulation of this land acknowledgment.

References

- Abers, G. A., MacKenzie, L. S., Rondenay, S., Zhang, Z., Wech, A. G., & Creager, K. C. (2009). Imaging the source region of Cascadia tremor and intermediate-depth earthquakes. *Geology*, *37*(12), 1119–1122. doi: 10.1130/g30143a.1
- Albuquerque Seismological Laboratory (ASL)/USGS. (1990). [Dataset] *United States national seismic network*. International Federation of Digital Seismograph Networks. doi: 10.7914/SN/US
- Albuquerque Seismological Laboratory/USGS. (2014). [Dataset] *Global seismograph network (GSN - IRIS/USGS)*. International Federation of Digital Seismograph Networks. doi: 10.7914/SN/IU
- Armbruster, J. G., Kim, W.-Y., & Rubin, A. M. (2014). Accurate tremor locations from coherent S and P waves. *Journal of Geophysical Research: Solid Earth*, *119*(6), 5000–5013. doi: 10.1002/2014jb011133
- Arnulf, A. F., Bassett, D., Harding, A. J., Kodaira, S., Nakanishi, A., & Moore, G. (2022). Upper-plate controls on subduction zone geometry, hydration and earthquake behaviour. *Nature Geoscience*, *15*(2), 143–148. doi: 10.1038/s41561-021-00879-x
- Aster, R. C., Borchers, B., & Thurber, C. H. (2018). *Parameter estimation and inverse problems*. Elsevier.
- Audet, P. (2020). [Dataset] *RfPy: Teleseismic receiver function calculation and post-processing*. Zenodo. doi: 10.5281/ZENODO.4302558
- Audet, P., & Bloch, W. (2022). [Dataset] *PyRaysum: Software for modeling ray-theoretical body-wave propagation*. Zenodo. doi: 10.5281/ZENODO.7468301
- Audet, P., Bostock, M. G., Boyarko, D. C., Brudzinski, M. R., & Allen, R. M. (2010). Slab morphology in the Cascadia fore arc and its relation to episodic tremor and slip. *Journal of Geophysical Research*, *115*. doi: 10.1029/2008jb006053
- Audet, P., Bostock, M. G., Christensen, N. I., & Peacock, S. M. (2009). Seismic evidence for overpressured subducted oceanic crust and megathrust fault sealing. *Nature*, *457*(7225), 76–78. doi: 10.1038/nature07650
- Audet, P., Bostock, M. G., Mercier, J.-P., & Cassidy, J. F. (2008). Morphology of the Explorer–Juan de Fuca slab edge in northern Cascadia: Imaging plate capture

- at a ridge-trench-transform triple junction. *Geology*, *36*(11), 895–898. Retrieved from <https://doi.org/10.1130/G25356A.1> doi: 10.1130/G25356A.1
- 575
576
577 Audet, P., & Schaeffer, A. J. (2018). Fluid pressure and shear zone development
578 over the locked to slow slip region in Cascadia. *Science Advances*, *4*(3), eaar2982.
579 doi: 10.1126/sciadv.aar2982
- 580 Bar, N., Long, M. D., Wagner, L. S., Beck, S. L., Zandt, G., & Tavera, H. (2019,
581 feb). Receiver function analysis reveals layered anisotropy in the crust and upper
582 mantle beneath southern Peru and northern Bolivia. *Tectonophysics*, *753*, 93–110.
583 doi: 10.1016/j.tecto.2019.01.007
- 584 Bloch, W., & Audet, P. (2023). PyRaysum: Software for modeling ray-theoretical
585 plane body-wave propagation in dipping anisotropic media. *Seismica*, *2*(1). doi:
586 10.26443/seismica.v2i1.220
- 587 Bloch, W., John, T., Kummerow, J., Salazar, P., Krüger, O. S., & Shapiro, S. A.
588 (2018). Watching dehydration: Seismic indication for transient fluid pathways
589 in the oceanic mantle of the subducting Nazca slab. *Geochemistry, Geophysics,*
590 *Geosystems*, *19*(9), 3189–3207. doi: 10.1029/2018gc007703
- 591 Bombardier, M., Dosso, S. E., Cassidy, J. F., & Kao, H. (2023). Tackling the
592 challenges of tectonic tremor localization using differential traveltimes and
593 Bayesian inversion. *Geophysical Journal International*, *234*(1), 479–493. doi:
594 10.1093/gji/ggad086
- 595 Bostock, M. G. (1998). Mantle stratigraphy and evolution of the Slave province.
596 *Journal of Geophysical Research: Solid Earth*, *103*(B9), 21183–21200. doi:
597 10.1029/98jb01069
- 598 Bostock, M. G., R., H., Rondenay, S., & Peacock, S. (2002). An inverted continen-
599 tal Moho and serpentinization of the forearc mantle. *Nature*, *417*, 536–538. doi:
600 <https://doi.org/10.1038/417536a>
- 601 Bostock, M. G., Thomas, A. M., Savard, G., Chuang, L., & Rubin, A. M. (2015).
602 Magnitudes and moment-duration scaling of low-frequency earthquakes beneath
603 southern Vancouver Island. *Journal of Geophysical Research: Solid Earth*, *120*(9),
604 6329–6350. doi: 10.1002/2015jb012195
- 605 Brandon, M. T., & Calderwood, A. R. (1990). High-pressure metamorphism and up-
606 lift of the Olympic subduction complex. *Geology*, *18*(12), 1252. doi: 10.1130/0091
607 -7613(1990)018(1252:hpmawo)2.3.co;2
- 608 Brodsky, E. (2001). [Dataset] *Observational constraints on persistent water level*
609 *changes generated by seismic waves*. International Federation of Digital Seismo-
610 graph Networks. doi: 10.7914/SN/YS_2001
- 611 Brudzinski, M., & Allen, R. (2007). [Dataset] *Resolving structural control of episodic*
612 *tremor and slip along the length of Cascadia*. International Federation of Digital
613 Seismograph Networks. doi: 10.7914/SN/YW_2007
- 614 Cakir, R. (2016). [Dataset] *Monitoring active faults for tectonic mapping efforts in*
615 *Washington state*. International Federation of Digital Seismograph Networks. doi:
616 10.7914/SN/X4_2016
- 617 Caldwell, W. B., Klempner, S. L., Lawrence, J. F., Rai, S. S., & Ashish. (2013,
618 apr). Characterizing the Main Himalayan Thrust in the Garhwal Himalaya, India
619 with receiver function CCP stacking. *Earth and Planetary Science Letters*, *367*,
620 15–27. doi: 10.1016/j.epsl.2013.02.009
- 621 Calvert, A. J. (1996). Seismic reflection constraints on imbrication and underplating
622 of the northern Cascadia convergent margin. *Canadian Journal of Earth Sciences*,
623 *33*(9), 1294–1307. doi: 10.1139/e96-098
- 624 Calvert, A. J. (2004). Seismic reflection imaging of two megathrust shear zones
625 in the northern Cascadia subduction zone. *Nature*, *428*(6979), 163–167. doi: 10
626 .1038/nature02372
- 627 Calvert, A. J., Bostock, M. G., Savard, G., & Unsworth, M. J. (2020). Cascadia low
628 frequency earthquakes at the base of an overpressured subduction shear zone. *Na-*

- 629 *ture Communications*, 11(1). doi: 10.1038/s41467-020-17609-3
- 630 Calvert, A. J., & Clowes, R. M. (1991). Seismic evidence for the migration of fluids
631 within the accretionary complex of western Canada. *Canadian Journal of Earth
632 Sciences*, 28(4), 542–556. doi: 10.1139/e91-048
- 633 Calvert, A. J., Preston, L. A., & Farahbod, A. M. (2011). Sedimentary underplat-
634 ing at the Cascadia mantle-wedge corner revealed by seismic imaging. *Nature Geo-
635 science*, 4(8), 545–548. doi: 10.1038/ngeo1195
- 636 Calvert, A. J., Ramachandran, K., Kao, H., & Fisher, M. A. (2006). Lo-
637 cal thickening of the Cascadia forearc crust and the origin of seismic reflec-
638 tors in the uppermost mantle. *Tectonophysics*, 420(1-2), 175–188. doi:
639 10.1016/j.tecto.2006.01.021
- 640 Carbotte, S. M., Boston, B., Han, S., Shuck, B., Canales, J. P., Beeson, J. W., ...
641 Tobin, H. J. (2022). New observations of plate interface depth and geometry at
642 the offshore Cascadia subduction zone from the CASIE21 and comparisons with existing plate depth models. In *Agu
643 fall meeting abstracts* (Vol. 2022, pp. S46B–01).
- 644 Carbotte, S. M., Han, S., Boston, B., & Canales, J. (2023). *Processed pre-stack
645 depth-migrated seismic reflection data from the 2021 CASIE21 multi-channel
646 seismic survey (MGL2104)*. Interdisciplinary Earth Data Alliance (IEDA). doi:
647 10.26022/IEDA/331274
- 648 Cascades Volcano Observatory/USGS. (2001). *[Dataset] Cascade chain volcano mon-
649 itoring*. International Federation of Digital Seismograph Networks. doi: 10.7914/
650 SN/CC
- 651 Cassidy, J. F., & Ellis, R. M. (1993). S wave velocity structure of the northern
652 Cascadia subduction zone. *Journal of Geophysical Research: Solid Earth*, 98(B3),
653 4407–4421. Retrieved from [https://agupubs.onlinelibrary.wiley.com/doi/
654 abs/10.1029/92JB02696](https://agupubs.onlinelibrary.wiley.com/doi/abs/10.1029/92JB02696) doi: <https://doi.org/10.1029/92JB02696>
- 655 Chaytor, J. D., Goldfinger, C., Dziak, R. P., & Fox, C. G. (2004). Active deforma-
656 tion of the Gorda plate: Constraining deformation models with new geophysical
657 data. *Geology*, 32(4), 353–356.
- 658 Chen, L., Wen, L., & Zheng, T. (2005, nov). A wave equation migration method for
659 receiver function imaging: 2. application to the Japan subduction zone. *Journal of
660 Geophysical Research: Solid Earth*, 110(B11). doi: 10.1029/2005jb003666
- 661 Christensen, N. I. (1984). Pore pressure and oceanic crustal seismic struc-
662 ture. *Geophysical Journal International*, 79(2), 411–423. doi: 10.1111/
663 j.1365-246x.1984.tb02232.x
- 664 Christensen, N. I. (1996). Poisson's ratio and crustal seismology. *Journal of Geo-
665 physical Research: Solid Earth*, 101(B2), 3139–3156. doi: 10.1029/95jb03446
- 666 Clarke, S. H. (1992). Geology of the Eel River basin and adjacent region:
667 Implications for late cenozoic tectonics of the southern Cascadia subduc-
668 tion zone and Mendocino triple junction (1). *AAPG Bulletin*, 76. doi:
669 10.1306/bdff87ae-1718-11d7-8645000102c1865d
- 670 Clowes, R. M., Brandon, M. T., Green, A. G., Yorath, C. J., Brown, A. S.,
671 Kanasewich, E. R., & Spencer, C. (1987). LITHOPROBE—southern Vancou-
672 ver island: Cenozoic subduction complex imaged by deep seismic reflections.
673 *Canadian Journal of Earth Sciences*, 24(1), 31–51. doi: 10.1139/e87-004
- 674 Clowes, R. M., Yorath, C., & Hyndman, R. (1987). Reflection mapping across the
675 convergent margin of western Canada. *Geophysical Journal International*, 89(1),
676 79–84. doi: 10.1111/j.1365-246x.1987.tb04391.x
- 677 Colavitti, L., Hetényi, G., & the AplArray Working Group. (2022, nov). A new
678 approach to construct 3-D crustal shear-wave velocity models: method descrip-
679 tion and application to the Central Alps. *Acta Geodaetica et Geophysica*, 57(4),
680 529–562. doi: 10.1007/s40328-022-00394-4
- 681 Cramer, F., Shephard, G. E., & Heron, P. J. (2020). The misuse of colour in sci-
682

- 683 ence communication. *Nature communications*, *11*(1), 1–10. doi: [https://doi.org/](https://doi.org/10.1038/s41467-020-19160-7)
684 10.1038/s41467-020-19160-7
- 685 Creager, K. (2014). [Dataset] *Collaborative research: Illuminating the architecture of*
686 *the greater Mount St. Helens magmatic systems from slab to surface*. International
687 Federation of Digital Seismograph Networks. doi: 10.7914/SN/XD_2014
- 688 Delph, J. R., Levander, A., & Niu, F. (2018). Fluid controls on the heteroge-
689 neous seismic characteristics of the Cascadia margin. *Geophysical Research Let-*
690 *ters*, *45*(20), 11,021–11,029. Retrieved from [https://agupubs.onlinelibrary](https://agupubs.onlinelibrary.wiley.com/doi/abs/10.1029/2018GL079518)
691 .[wiley.com/doi/abs/10.1029/2018GL079518](https://agupubs.onlinelibrary.wiley.com/doi/abs/10.1029/2018GL079518) doi: [https://doi.org/10.1029/](https://doi.org/10.1029/2018GL079518)
692 2018GL079518
- 693 Delph, J. R., Thomas, A. M., & Levander, A. (2021). Subcretionary tecton-
694 ics: Linking variability in the expression of subduction along the Cascadia
695 forearc. *Earth and Planetary Science Letters*, *556*, 116724. Retrieved from
696 <https://www.sciencedirect.com/science/article/pii/S0012821X20306683>
697 doi: <https://doi.org/10.1016/j.epsl.2020.116724>
- 698 DeMets, C., Gordon, R. G., Argus, D. F., & Stein, S. (1994). Effect of recent revi-
699 sions to the geomagnetic reversal time scale on estimates of current plate motions.
700 *Geophysical Research Letters*, *21*(20), 2191–2194. doi: 10.1029/94gl02118
- 701 Dragert, H., Wang, K., & James, T. S. (2001). A silent slip event on the deeper Cas-
702 cadia subduction interface. *Science*, *292*(5521), 1525–1528. doi: 10.1126/science
703 .1060152
- 704 Dragert, H., Wang, K., & Rogers, G. (2004). Geodetic and seismic signatures of
705 episodic tremor and slip in the northern Cascadia subduction zone. *Earth, Planets*
706 *and Space*, *56*(12), 1143–1150. doi: 10.1186/bf03353333
- 707 Egbert, G. D., Yang, B., Bedrosian, P. A., Key, K., Livelybrooks, D. W., Schultz,
708 A., ... Parris, B. (2022). Fluid transport and storage in the Cascadia forearc
709 influenced by overriding plate lithology. *Nature Geoscience*, *15*(8), 677–682. doi:
710 10.1038/s41561-022-00981-8
- 711 Flueh, E. R., Fisher, M. A., Bialas, J., Childs, J. R., Klaeschen, D., Kukowski,
712 N., ... Vidal, N. (1998). New seismic images of the Cascadia subduction
713 zone from cruise SO108 — ORWELL. *Tectonophysics*, *293*(1-2), 69–84. doi:
714 10.1016/s0040-1951(98)00091-2
- 715 Flück, P., Hyndman, R. D., & Wang, K. (1997). Three-dimensional dislocation
716 model for great earthquakes of the Cascadia subduction zone. *Journal of Geophys-*
717 *ical Research: Solid Earth*, *102*(B9), 20539–20550. doi: 10.1029/97jb01642
- 718 Frederiksen, A. W., & Bostock, M. G. (2000). Modelling teleseismic waves in dip-
719 ping anisotropic structures. *Geophysical Journal International*, *141*(2), 401–412.
720 doi: 10.1046/j.1365-246x.2000.00090.x
- 721 Gulick, S. P. S., Meltzer, A. M., & Clarke, S. H. (1998). Seismic structure of the
722 southern Cascadia subduction zone and accretionary prism north of the Mendo-
723 cino triple junction. *Journal of Geophysical Research: Solid Earth*, *103*(B11),
724 27207–27222. doi: 10.1029/98jb02526
- 725 Guo, H., McGuire, J. J., & Zhang, H. (2021). Correlation of porosity variations and
726 rheological transitions on the southern Cascadia megathrust. *Nature Geoscience*,
727 *14*(5), 341–348. doi: 10.1038/s41561-021-00740-1
- 728 Gurrola, H., Baker, G. E., & Minster, J. B. (1995). Simultaneous time-domain de-
729 convolution with application to the computation of receiver functions. *Geophysical*
730 *Journal International*, *120*(3), 537–543.
- 731 Han, S., Carbotte, S. M., Canales, J. P., Nedimović, M. R., Carton, H., Gibson,
732 J. C., & Horning, G. W. (2016). Seismic reflection imaging of the Juan de Fuca
733 plate from ridge to trench: New constraints on the distribution of faulting and
734 evolution of the crust prior to subduction. *Journal of Geophysical Research: Solid*
735 *Earth*, *121*(3), 1849–1872. doi: 10.1002/2015jb012416
- 736 Hansen, R. T., Bostock, M. G., & Christensen, N. I. (2012). Nature of the low veloc-

- ity zone in Cascadia from receiver function waveform inversion. *Earth and Planetary Science Letters*, 337-338, 25–38. doi: 10.1016/j.epsl.2012.05.031
- Harris, C. R., Millman, K. J., van der Walt, S. J., Gommers, R., Virtanen, P., Cournapeau, D., . . . Oliphant, T. E. (2020). Array programming with NumPy. *Nature*, 585(7825), 357–362. doi: 10.1038/s41586-020-2649-2
- Hayes, G. P., Moore, G. L., Portner, D. E., Hearne, M., Flamme, H., Furtney, M., & Smoczyk, G. M. (2018). Slab2, a comprehensive subduction zone geometry model. *Science*, 362(6410), 58–61. doi: 10.1126/science.aat4723
- Hunter, J. D. (2007). Matplotlib: A 2D graphics environment. *Computing in Science & Engineering*, 9(3), 90–95. doi: 10.1109/MCSE.2007.55
- Ichinose, G. A., Thio, H. K., & Somerville, P. G. (2004). Rupture process and near-source shaking of the 1965 Seattle-Tacoma and 2001 Nisqually, intraslab earthquakes. *Geophysical Research Letters*, 31(10). doi: 10.1029/2004gl019668
- International Seismological Centre. (2023). *ISC-GEM earthquake catalogue*. International Seismological Centre. doi: 10.31905/d808b825
- IRIS Transportable Array. (2003). *[Dataset] USArray transportable array*. International Federation of Digital Seismograph Networks. doi: 10.7914/SN/TA
- Kan, L.-Y., Chevrot, S., & Monteiller, V. (2023). Dehydration of the subducting Juan de Fuca plate and fluid pathways revealed by full waveform inversion of teleseismic P and SH waves in central Oregon. *Journal of Geophysical Research: Solid Earth*. doi: 10.1029/2022jb025506
- Kao, H., Shan, S.-J., Dragert, H., Rogers, G., Cassidy, J. F., & Ramachandran, K. (2005, aug). A wide depth distribution of seismic tremors along the northern Cascadia margin. *Nature*, 436(7052), 841–844. doi: 10.1038/nature03903
- Kao, H., Wang, K., Chen, R.-Y., Wada, I., He, J., & Malone, S. D. (2008). Identifying the rupture plane of the 2001 Nisqually, Washington, earthquake. *Bulletin of the Seismological Society of America*, 98(3), 1546–1558.
- Kao, H., Wang, K., Dragert, H., Kao, J. Y., & Rogers, G. (2010). Estimating seismic moment magnitude (Mw) of tremor bursts in northern Cascadia: Implications for the “seismic efficiency” of episodic tremor and slip. *Geophysical Research Letters*, 37(19). doi: 10.1029/2010gl044927
- Keach, R. W., Oliver, J. E., Brown, L. D., & Kaufman, S. (1989). Cenozoic active margin and shallow cascades structure: COCORP results from western Oregon. *Geological Society of America Bulletin*, 101(6), 783–794. doi: 10.1130/0016-7606(1989)101<0783:camasc>2.3.co;2
- Kennett, B. L. N. (1991). The removal of free surface interactions from three-component seismograms. *Geophysical Journal International*, 104(1), 153–154. doi: 10.1111/j.1365-246x.1991.tb02501.x
- Kirkpatrick, S., Gelatt, C. D., & Vecchi, M. P. (1983, may). Optimization by simulated annealing. *Science*, 220(4598), 671–680. doi: 10.1126/science.220.4598.671
- Krischer, L., Megies, T., Barsch, R., Beyreuther, M., Lecocq, T., Caudron, C., & Wassermann, J. (2015). ObsPy: a bridge for seismology into the scientific Python ecosystem. *Computational Science Discovery*, 8(1), 014003. doi: 10.1088/1749-4699/8/1/014003
- Langston, C. A., & Blum, D. E. (1977). The April 29, 1965, Puget sound earthquake and the crustal and upper mantle structure of western Washington. *Bulletin of the Seismological Society of America*, 67(3), 693–711. doi: 10.1785/bssa0670030693
- Levander, A. (2007). *[Dataset] Seismic and geodetic investigations of Mendocino triple junction dynamics*. International Federation of Digital Seismograph Networks. doi: 10.7914/SN/XQ_2007
- Li, X., Sobolev, S., Kind, R., Yuan, X., & Estabrook, C. (2000, dec). A detailed receiver function image of the upper mantle discontinuities in the Japan subduction zone. *Earth and Planetary Science Letters*, 183(3-4), 527–541. doi: 10.1016/s0012-821x(00)00294-6

- 791 Liu, D., Zhao, L., Paul, A., Yuan, H., Solarino, S., Aubert, C., . . . Guillot, S. (2022,
792 jan). Receiver function mapping of the mantle transition zone beneath the West-
793 ern Alps: New constraints on slab subduction and mantle upwelling. *Earth and*
794 *Planetary Science Letters*, 577, 117267. doi: 10.1016/j.epsl.2021.117267
- 795 Luo, Y., & Liu, Z. (2021, mar). Fault zone heterogeneities explain depth-dependent
796 pattern and evolution of slow earthquakes in Cascadia. *Nature Communications*,
797 12(1). doi: 10.1038/s41467-021-22232-x
- 798 MacKay, M. E., Moore, G. F., Cochrane, G. R., Moore, J. C., & Kulm, L. D. (1992).
799 Landward vergence and oblique structural trends in the Oregon margin accre-
800 tionary prism: Implications and effect on fluid flow. *Earth and Planetary Science*
801 *Letters*, 109(3-4), 477–491. doi: 10.1016/0012-821x(92)90108-8
- 802 Malone, S., Creager, K., Rondenay, S., Melbourne, T., & Abers, G. (2006). [Dataset]
803 *Collaborative research: Earthscope integrated investigations of Cascadia subduction*
804 *zone tremor, structure and process*. International Federation of Digital Seismo-
805 graph Networks. doi: 10.7914/SN/XU_2006
- 806 Mann, M. E., Abers, G. A., Crosbie, K., Creager, K., Ulberg, C., Moran, S., & Ron-
807 denay, S. (2019). Imaging subduction beneath Mount St. Helens: Implications
808 for slab dehydration and magma transport. *Geophysical Research Letters*, 46(6),
809 3163–3171. Retrieved from [https://agupubs.onlinelibrary.wiley.com/doi/](https://agupubs.onlinelibrary.wiley.com/doi/abs/10.1029/2018GL081471)
810 [abs/10.1029/2018GL081471](https://doi.org/10.1029/2018GL081471) doi: <https://doi.org/10.1029/2018GL081471>
- 811 McCrory, P. A., Blair, J. L., Oppenheimer, D. H., & Walter, S. R. (2004). *Depth to*
812 *the Juan de Fuca slab beneath the Cascadia subduction margin— a 3-D model for*
813 *sorting earthquakes*. US Geological Survey. doi: 10.3133/ds91
- 814 McCrory, P. A., Blair, J. L., Waldhauser, F., & Oppenheimer, D. H. (2012). Juan
815 de Fuca slab geometry and its relation to Wadati-Benioff zone seismicity. *Journal*
816 *of Geophysical Research: Solid Earth*, 117(B9). doi: 10.1029/2012jb009407
- 817 McGary, R. S., Evans, R. L., Wannamaker, P. E., Elsenbeck, J., & Rondenay, S.
818 (2014). Pathway from subducting slab to surface for melt and fluids beneath
819 Mount Rainier. *Nature*, 511(7509), 338–340.
- 820 Merrill, R., Bostock, M. G., Peacock, S. M., Calvert, A. J., & Christensen, N. I.
821 (2020). A double difference tomography study of the Washington forearc: Does
822 Siletzia control crustal seismicity? *Journal of Geophysical Research: Solid Earth*,
823 125(10). doi: 10.1029/2020jb019750
- 824 Merrill, R., Bostock, M. G., Peacock, S. M., Schaeffer, A. J., & Roecker, S. W.
825 (2022). Complex structure in the Nootka fault zone revealed by double-difference
826 tomography and a new earthquake catalog. *Geochemistry, Geophysics, Geosys-*
827 *tems*, 23(2). doi: 10.1029/2021gc010205
- 828 Michailos, K., Hetényi, G., Scarponi, M., Stipčević, J., Bianchi, I., Bonatto, L., . . .
829 and, J. V. (2023, may). Moho depths beneath the European Alps: a homoge-
830 neously processed map and receiver functions database. *Earth System Science*
831 *Data*, 15(5), 2117–2138. doi: 10.5194/essd-15-2117-2023
- 832 Mitchell, C. E., Vincent, P., Weldon, R. J., & Richards, M. A. (1994). Present-
833 day vertical deformation of the Cascadia margin, Pacific northwest, United
834 States. *Journal of Geophysical Research: Solid Earth*, 99(B6), 12257–12277.
835 doi: 10.1029/94jb00279
- 836 Morton, E. A., Bilek, S. L., & Rowe, C. A. (2023). Cascadia subduction zone fault
837 heterogeneities from newly detected small magnitude earthquakes. *Journal of Geo-*
838 *physical Research: Solid Earth*. doi: 10.1029/2023jb026607
- 839 Nabelek, J., Li, X., Azevedo, S., Braunmiller, J., Fabritius, A., Leitner, B., . . .
840 Zandt, G. (1993). A high-resolution image of the Cascadia subduction zone
841 from teleseismic converted phases recorded by a broadband seismic array. *Eos*
842 *Trans. AGU*, 74(43), 431.
- 843 Natural Resources Canada (NRCAN Canada). (1975). [Dataset] *Canadian national*
844 *seismograph network*. International Federation of Digital Seismograph Networks.

- 845 doi: 10.7914/SN/CN
- 846 Nedimović, M. R., Bohnenstiehl, D. R., Carbotte, S. M., Canales, J. P., & Dziak,
847 R. P. (2009). Faulting and hydration of the Juan de Fuca plate system. *Earth and*
848 *Planetary Science Letters*, *284*(1-2), 94–102. doi: 10.1016/j.epsl.2009.04.013
- 849 Nedimović, M. R., Hyndman, R. D., Ramachandran, K., & Spence, G. D. (2003).
850 Reflection signature of seismic and aseismic slip on the northern Cascadia subduc-
851 tion interface. *Nature*, *424*(6947), 416–420. doi: 10.1038/nature01840
- 852 Nicholson, T., Bostock, M., & Cassidy, J. F. (2005). New constraints on subduction
853 zone structure in northern Cascadia. *Geophysical Journal International*, *161*(3),
854 849–859. Retrieved from <https://doi.org/10.1111/j.1365-246X.2005.02605.x>
855 doi: 10.1111/j.1365-246X.2005.02605.x
- 856 Niu, F., Levander, A., Ham, S., & Obayashi, M. (2005, oct). Mapping the subduct-
857 ing Pacific slab beneath southwest Japan with Hi-net receiver functions. *Earth*
858 *and Planetary Science Letters*, *239*(1-2), 9–17. doi: 10.1016/j.epsl.2005.08.009
- 859 Northern California Earthquake Data Center. (2014). [Dataset] *Berkeley digital seis-*
860 *mic network (BDSN)*. Northern California Earthquake Data Center. doi: 10.7932/
861 BDSN
- 862 Nuttli, O. W. (1952). The western Washington earthquake of April 13, 1949.
863 *Bulletin of the Seismological Society of America*, *42*(1), 21–28. doi: 10.1785/
864 bssa0420010021
- 865 Plourde, A. P., Bostock, M. G., Audet, P., & Thomas, A. M. (2015). Low-frequency
866 earthquakes at the southern Cascadia margin. *Geophysical Research Letters*,
867 *42*(12), 4849–4855. doi: 10.1002/2015gl064363
- 868 Riddihough, R. (1984, aug). Recent movements of the Juan de Fuca plate system.
869 *Journal of Geophysical Research: Solid Earth*, *89*(B8), 6980–6994. doi: 10.1029/
870 jb089ib08p06980
- 871 Rodriguez, E., & Russo, R. (2019, dec). Southern Chile crustal structure from tele-
872 seismic receiver functions: Responses to ridge subduction and terrane assembly of
873 Patagonia. *Geosphere*, *16*(1), 378–391. doi: 10.1130/ges01692.1
- 874 Rohr, K. M., Furlong, K. P., & Riedel, M. (2018). Initiation of strike-slip faults,
875 serpentization, and methane: The Nootka fault zone, the Juan de Fuca-Explorer
876 plate boundary. *Geochemistry, Geophysics, Geosystems*, *19*(11), 4290–4312.
- 877 Rondenay, S., Bostock, M. G., & Shragge, J. (2001). Multiparameter two-
878 dimensional inversion of scattered teleseismic body waves 3. application to the
879 Cascadia 1993 data set. *Journal of Geophysical Research: Solid Earth*, *106*(B12),
880 30795–30807. doi: 10.1029/2000jb000039
- 881 Royer, A., & Bostock, M. (2014). A comparative study of low frequency earthquake
882 templates in northern Cascadia. *Earth and Planetary Science Letters*, *402*, 247–
883 256. doi: 10.1016/j.epsl.2013.08.040
- 884 Sandwell, D. T. (1987). Biharmonic spline interpolation of GEOS-3 and
885 SEASAT altimeter data. *Geophysical Research Letters*, *14*(2), 139–142. doi:
886 10.1029/gl014i002p00139
- 887 Savard, G., Bostock, M. G., & Christensen, N. I. (2018). Seismicity, metamor-
888 phism, and fluid evolution across the northern Cascadia fore arc. *Geochemistry,*
889 *Geophysics, Geosystems*, *19*(6), 1881–1897. doi: 10.1029/2017gc007417
- 890 Savard, G., Bostock, M. G., Hutchinson, J., Kao, H., Christensen, N. I., & Pea-
891 cock, S. M. (2020). The northern terminus of Cascadia subduction. *Journal of*
892 *Geophysical Research: Solid Earth*, *125*(6). doi: 10.1029/2019jb018453
- 893 Singer, J., Kissling, E., Diehl, T., & Hetényi, G. (2017, feb). The underthrusting
894 Indian crust and its role in collision dynamics of the Eastern Himalaya in Bhutan:
895 Insights from receiver function imaging. *Journal of Geophysical Research: Solid*
896 *Earth*, *122*(2), 1152–1178. doi: 10.1002/2016jb013337
- 897 Song, T.-R. A., Helmberger, D. V., Brudzinski, M. R., Clayton, R. W., Davis, P.,
898 Pérez-Campos, X., & Singh, S. K. (2009). Subducting slab ultra-slow velocity

- 899 layer coincident with silent earthquakes in southern Mexico. *Science*, *324*(5926),
900 502–506. doi: 10.1126/science.1167595
- 901 Subedi, S., Hetényi, G., Vergne, J., Bollinger, L., Lyon-Caen, H., Farra, V., ...
902 Gupta, R. M. (2018, dec). Imaging the Moho and the Main Himalayan Thrust in
903 western Nepal with receiver functions. *Geophysical Research Letters*, *45*(24). doi:
904 10.1029/2018gl080911
- 905 Tauzin, B., Bodin, T., Debayle, E., Perrillat, J.-P., & Reynard, B. (2016). Multi-
906 mode conversion imaging of the subducted Gorda and Juan de Fuca plates below
907 the north American continent. *Earth and Planetary Science Letters*, *440*, 135-
908 146. Retrieved from [https://www.sciencedirect.com/science/article/pii/
909 S0012821X16300115](https://www.sciencedirect.com/science/article/pii/S0012821X16300115) doi: <https://doi.org/10.1016/j.epsl.2016.01.036>
- 910 Trehu, A., & Williams, M. (2008). [Dataset] *Central Oregon locked zone ar-
911 ray, monitoring seismicity associated with a possible asperity on the Cascadia
912 megathrust*. International Federation of Digital Seismograph Networks. doi:
913 10.7914/SN/XA_2008
- 914 Tréhu, A. M., Asudeh, I., Brocher, T. M., Luetgert, J. H., Mooney, W. D., Nabelek,
915 J. L., & Nakamura, Y. (1994). Crustal architecture of the Cascadia forearc.
916 *Science*, *266*(5183), 237–243. doi: 10.1126/science.266.5183.237
- 917 Tréhu, A. M., Blakely, R. J., & Williams, M. C. (2012). Subducted seamounts and
918 recent earthquakes beneath the central Cascadia forearc. *Geology*, *40*(2), 103–106.
919 doi: 10.1130/g32460.1
- 920 Uieda, L., Tian, D., Leong, W. J., Schlitzer, W., Grund, M., Jones, M., ... Wes-
921 sel, P. (2023). *PyGMT: A Python interface for the Generic Mapping Tools*.
922 Zenodo. Retrieved from <https://doi.org/10.5281/zenodo.7772533> doi:
923 10.5281/zenodo.7772533
- 924 University of Oregon. (1990). [Dataset] *Pacific northwest seismic network - Univer-
925 sity of Oregon*. International Federation of Digital Seismograph Networks. doi: 10
926 .7914/SN/UO
- 927 University of Washington. (1963). [Dataset] *Pacific northwest seismic network -
928 University of Washington*. International Federation of Digital Seismograph Net-
929 works. doi: 10.7914/SN/UW
- 930 USGS Menlo Park. (1966). [Dataset] *USGS Northern California seismic network*.
931 International Federation of Digital Seismograph Networks. doi: 10.7914/SN/NC
- 932 Virtanen, P., Gommers, R., Oliphant, T. E., Haberland, M., Reddy, T., Courn-
933 peau, D., ... SciPy 1.0 Contributors (2020). SciPy 1.0: Fundamental Algo-
934 rithms for Scientific Computing in Python. *Nature Methods*, *17*, 261–272. doi:
935 10.1038/s41592-019-0686-2
- 936 Waldhauser, F. (2009). Near-real-time double-difference event location using long-
937 term seismic archives, with application to northern California. *Bulletin of the
938 Seismological Society of America*, *99*(5), 2736–2748. doi: 10.1785/0120080294
- 939 Wang, K., & Rogers, G. C. (1994). An explanation for the double seismic layers
940 north of the Mendocino triple junction. *Geophysical Research Letters*, *21*(2), 121–
941 124. doi: 10.1029/93gl03538
- 942 Watt, J. T., & Brothers, D. S. (2020). Systematic characterization of morphotec-
943 tonic variability along the Cascadia convergent margin: Implications for shallow
944 megathrust behavior and tsunami hazards. *Geosphere*, *17*(1), 95–117. doi:
945 10.1130/ges02178.1
- 946 Wech, A. G. (2010). [dataset] Interactive tremor monitoring. *Seismological Research
947 Letters*, *81*(4), 664–669. doi: 10.1785/gssrl.81.4.664
- 948 Wech, A. G., & Creager, K. C. (2011, aug). A continuum of stress, strength and slip
949 in the Cascadia subduction zone. *Nature Geoscience*, *4*(9), 624–628. doi: 10.1038/
950 ngeo1215
- 951 Wells, R., Bukry, D., Friedman, R., Pyle, D., Duncan, R., Haeussler, P., & Wooden,
952 J. (2014). Geologic history of Siletzia, a large igneous province in the Oregon and

- 953 Washington coast range: Correlation to the geomagnetic polarity time scale and
954 implications for a long-lived yellowstone hotspot. *Geosphere*, 10(4), 692–719. doi:
955 10.1130/ges01018.1
- 956 Wells, R., Weaver, C. S., & Blakely, R. J. (1998). Fore-arc migration in Cas-
957 cadia and its neotectonic significance. *Geology*, 26(8), 759. doi: 10.1130/
958 0091-7613(1998)026<0759:famica>2.3.co;2
- 959 Wessel, P., & Becker, J. M. (2008, jul). Interpolation using a generalized Green's
960 function for a spherical surface spline in tension. *Geophysical Journal Interna-*
961 *tional*, 174(1), 21–28. doi: 10.1111/j.1365-246x.2008.03829.x
- 962 Wessel, P., Luis, J. F., Uieda, L., Scharroo, R., Wobbe, F., Smith, W. H. F., & Tian,
963 D. (2019). The Generic Mapping Tools version 6. *Geochemistry, Geophysics,*
964 *Geosystems*, 20(11), 5556–5564. doi: 10.1029/2019gc008515
- 965 Wilson, D. S. (1989). Deformation of the so-called Gorda plate. *Journal of Geophys-*
966 *ical Research: Solid Earth*, 94(B3), 3065–3075. doi: 10.1029/jb094ib03p03065
- 967 Wilson, D. S. (1993). Confidence intervals for motion and deformation of the Juan
968 de Fuca plate. *Journal of Geophysical Research*, 98(B9), 16053. doi: 10.1029/
969 93jb01227
- 970 Xiang, Y., Sun, D., Fan, W., & Gong, X. (1997). Generalized simulated annealing
971 algorithm and its application to the Thomson model. *Physics Letters A*, 233(3),
972 216–220. doi: 10.1016/s0375-9601(97)00474-x
- 973 Xu, Q., Zhao, J., Yuan, X., Liu, H., Ju, C., Schurr, B., & Bloch, W. (2021, may).
974 Deep crustal contact between the Pamir and Tarim basin deduced from receiver
975 functions. *Geophysical Research Letters*, 48(9). doi: 10.1029/2021gl093271
- 976 Yuan, X., Sobolev, S. V., Kind, R., Oncken, O., Bock, G., Asch, G., . . . Comte, D.
977 (2000, dec). Subduction and collision processes in the Central Andes constrained
978 by converted seismic phases. *Nature*, 408(6815), 958–961. doi: 10.1038/35050073